



NUMERICAL STUDY OF OPTICAL DELAY IN SEMICONDUCTOR
MULTILAYER DISTRIBUTED BRAGG REFLECTOR AND TUNABLE
MICROCAVITY STRUCTURES

THESIS

Michael I. K. Etan, 2d Lt, USAF

AFIT/GE/ENG/01M-9

DEPARTMENT OF THE AIR FORCE
AIR UNIVERSITY
AIR FORCE INSTITUTE OF TECHNOLOGY

Wright-Patterson Air Force Base, Ohio

APPROVED FOR PUBLIC RELEASE; DISTRIBUTION UNLIMITED.

20010706 133

REPORT DOCUMENTATION PAGE				<i>Form Approved</i> OMB No. 074-0188	
The public reporting burden for this collection of information is estimated to average 1 hour per response, including the time for reviewing instructions, searching existing data sources, gathering and maintaining the data needed, and completing and reviewing the collection of information. Send comments regarding this burden estimate or any other aspect of the collection of information, including suggestions for reducing this burden to Department of Defense, Washington Headquarters Services, Directorate for Information Operations and Reports (0704-0188), 1215 Jefferson Davis Highway, Suite 1204, Arlington, VA 22202-4302. Respondents should be aware that notwithstanding any other provision of law, no person shall be subject to a penalty for failing to comply with a collection of information if it does not display a currently valid OMB control number. PLEASE DO NOT RETURN YOUR FORM TO THE ABOVE ADDRESS.					
1. REPORT DATE (DD-MM-YYYY) 07-03-2001		2. REPORT TYPE Master's Thesis		3. DATES COVERED (From - To) Aug 2000 - Mar 2001	
4. TITLE AND SUBTITLE NUMERICAL STUDY OF OPTICAL DELAY IN SEMICONDUCTOR MULTILAYER DISTRIBUTED BRAGG REFLECTOR AND TUNABLE MICROCAVITY STRUCTURES				5a. CONTRACT NUMBER 5b. GRANT NUMBER 5c. PROGRAM ELEMENT NUMBER	
6. AUTHOR(S) Etan, Michael, I. K., 2d Lt, USAF				5d. PROJECT NUMBER 5e. TASK NUMBER 5f. WORK UNIT NUMBER	
7. PERFORMING ORGANIZATION NAMES(S) AND ADDRESS(S) Air Force Institute of Technology Graduate School of Electrical Engineering (AFIT/ENG) 2950 P Street, Building 640 WPAFB OH 45433-7765				8. PERFORMING ORGANIZATION REPORT NUMBER AFIT/GE/ENG/01M-9	
9. SPONSORING/MONITORING AGENCY NAME(S) AND ADDRESS(ES) AFRL/SNDD Attn: Dr. Thomas Nelson 13 th Street, Building 620 WPAFB OH 45433-7765 (937) 255-1874 x 3512				10. SPONSOR/MONITOR'S ACRONYM(S) 11. SPONSOR/MONITOR'S REPORT NUMBER(S)	
12. DISTRIBUTION/AVAILABILITY STATEMENT APPROVED FOR PUBLIC RELEASE; DISTRIBUTION UNLIMITED.					
13. SUPPLEMENTARY NOTES					
14. ABSTRACT The Air Force has a growing need for the greater bandwidth, speed, and flexibility offered by optical communication links. Future space systems and airborne platforms will most likely use optical signals for efficient power transmission and to minimize the possibility of spoofing and eavesdropping. Tunable optical delays play an important role in the implementation of free space optical communication links. The primary challenge in implementing these systems is the active maintenance of coherent wave fronts across the system's optical aperture. For space applications, this aperture may be hundreds of meters in diameter. Spatial segmentation of a large aperture into smaller elements is one approach that can be used to solve the problem of coherent waveform maintenance. In this research I explore three methods of achieving electrically tunable optical delay in a semiconductor structure. My first approach entails the use of multiple quantum wells inserted within the high index layers of a distributed Bragg reflector (DBR) to produce tunable optical delay when a transverse electric field is applied across the DBR. The second approach uses a cantilever mounted on top of a DBR structure. The cantilever is also a DBR and is used to vary the thickness of an air gap within the structure. A third approach relies on changing the angle of incidence of light on a DBR structure to produce a delay. All three methods produce acceptable results.					
15. SUBJECT TERMS Quantum Confined Stark Effect, Tunable Optical Pulse Delay, Group Delay, Quantum Wells, Distributed Bragg Reflector, Optical Filter					
16. SECURITY CLASSIFICATION OF:			17. LIMITATION OF ABSTRACT		18. NUMBER OF PAGES
a. REPORT U	b. ABSTRACT U	c. THIS PAGE U	UU		101
19a. NAME OF RESPONSIBLE PERSON Lt Col James A. Lott			19b. TELEPHONE NUMBER (Include area code) (937) 255-3636, ext 4576		

Standard Form 298 (Rev. 8-98)
 Prescribed by ANSI Std. Z39-18

	<i>Form Approved</i> OMB No. 074-0188
--	---

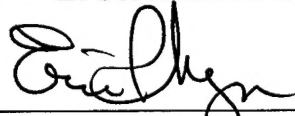
NUMERICAL STUDY OF OPTICAL DELAY IN SEMICONDUCTOR
MULTILAYER DISTRIBUTED BRAGG REFLECTOR AND TUNABLE
MICROCAVITY STRUCTURES

Michael I. K. Etan, B.S.
2d Lt, USAF

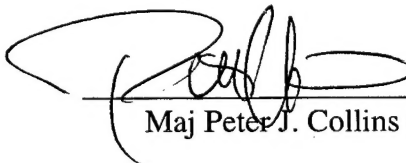
Approved:


Lt Col James A. Lott (Chairman)

07/MAR 01
date


Maj Eric P. Magee (Member)

7 MAR 01
date


Maj Peter J. Collins (Member)

7 MAR 01
date

The views expressed in this thesis are those of the author and do not reflect the official policy or position of the United States Air Force, Department of Defense, or the U. S. Government.

AFIT/GE/ENG/01M-9

NUMERICAL STUDY OF OPTICAL DELAY IN SEMICONDUCTOR
MULTILAYER DISTRIBUTED BRAGG REFLECTOR AND TUNABLE
MICROCAVITY STRUCTURES

THESIS

Presented to the Faculty

Department of Electrical and Computer Engineering

Graduate School of Engineering and Management

Air Force Institute of Technology

Air University

Air Education and Training Command

In Partial Fulfillment of the Requirements for the
Degree of Master of Science in Electrical Engineering

Michael I. K. Etan, B.S.

2d Lt, USAF

March 2001

APPROVED FOR PUBLIC RELEASE; DISTRIBUTION UNLIMITED.

Acknowledgement

I would like to express sincere appreciation to my Thesis Advisor Lt Col James A. Lott for his guidance and support throughout the course of this thesis. His ideas and extensive experience was a tremendous help. Thanks to Maj Peter J. Collins and Maj Eric P. Magee for careful reading of this manuscript and constructive and insightful comments.

I am also indebted to all the people at the laser device group at AFRL for their assistance and partnership in this project.

And finally, I thank my wife Yvette, for being there when it really mattered.

Michael I. K. Etan

Table of Contents

Acknowledgment.....	iv
List of Figures	vii
Abstract.....	x
1.0 Introduction	1-1
1.1 Motivation.....	1-1
1.2 Overview.....	1-8
1.3 Scope.....	1-14
1.4 Approach.....	1-14
1.5 Results.....	1-14
1.6 Summary.....	1-15
1.7 References.....	1-16
2.0 Background	
2.1 Introduction.....	2-1
2.2 DBR Structure.....	2-1
2.3 Mirror Design Using the Transmission Matrix Design.....	2-2
2.3.1 Band Pass Filter Design.....	2-9
2.4 Group and Phase Velocity in a DBR.....	2-10
2.5 Excitonic Transitions and Absorption.....	2-12
2.5.1 Bulk Material.....	2-12
2.5.2 Uncoupled Quantum Wells.....	2-13
2.5.3 Coupled Asymmetric Quantum Wells.....	2-16
2.6 Quantum Confined Stark Effect (QCSE).....	2-16
2.7 The Kramers-Kronig Relations.....	2-18
2.8 Optimum Quantum Well Structure.....	2-21
2.9 Delay Calculations.....	2-21
2.10 References.....	2-22
3.0 Modeling	
3.1 Introduction.....	3-1
3.2 Index of Refraction.....	3-1
3.3 Reflectance and Transmission Amplitude and Phase.....	3-3
3.4 Pulse and Delay.....	3-5
3.5 References.....	3-6
4.0 Device Design	
4.1 Introduction.....	4-1

4.2 Multiple Quantum Well filter Designs.....	4-1
4.3 Variable Angle of Incidence Device.....	4-7
4.4 Variable Air Gap Device.....	4-10

5.0 Results and Analysis

5.1 Introduction.....	5-1
5.2 Distortion in Dispersive Media.....	5-1
5.3 Multiple Quantum Well Design.....	5-3
5.4 Simulations for Variable Air Gap Designs.....	5-8
5.5 Variable Angle Structure.....	5-14

6.0 Conclusions

6.1 Introduction.....	6-1
6.2 Synopsis of Methods.....	6-2
6.3 Suggested Improvements and Further Research.....	6-3

List of Figures

Figures	Page
Figure 1-1: Air-to-air and air-to-ground application of optical delay	1-3
Figure 1-2: Space application of optical delay	1-3
Figure 1-3: Schematic of a pulse delayed by a DBR structure	1-5
Figure 1-4: Schematic of beam steering using unequal optical delay.....	1-5
Figure 1-5: Period of optical delay element with 3QWs	1-7
Figure 1-6: Schematic of p-i-n optical delay element under reverse bias	1-8
Figure 1-7: Single and double cantilever structures	1-9
Figure 2-1: Schematic of a DBR with embedded quantum wells	2-3
Figure 2-2: Reflectance verses Wavelength for 0 through 40 period DBRs	2-4
Figure 2-3: Reflectance and reflectivity phase for a 20 period DBR	2-5
Figure 2-4: Geometry for reflected fields in a multilayer stack.....	2-6
Figure 2-5: Absorption coefficient measured near the band edge of GaAs	2-14
Figure 2-6: Quantum well energy diagram	2-14
Figure 2-7: Calculated transitions for GaAs using at 300°K	2-15
Figure 2-8: Effects of electric field on quantum wells	2-17
Figure 2-9: Electric field dependence of absorption	2-19
Figure 2-10: Schematic of possible absorption change with wavelength.....	2-22
Figure 2-11: Five step asymmetric coupled quantum well	2-22
Figure 2-12: Electric field dependence of five step asymmetric coupled QW	2-23
Figure 2-13: Refractive index change for quantum wells	2-23

Figure 2-14: Reflectance spectra for GaAs/AlAs DBR with $\text{In}_{0.2}\text{Ga}_{0.8}\text{As}$ QWs	2-26
Figure 3-1: Refractive Index data for AlGaAs	3-2
Figure 3.2: Reflectance and transmittance amplitude and phase for a DBR	3-4
Figure 3-3: Input pulse and output pulse after a π linear phase	3-7
Figure 4-1: Reflectivity spectrum for various Fabry-Perot etalon structures	4-3
Figure 4-2: Reflectance and phase for filters after 2% increase in index.....	4-6
Figure 4-3: 3 Reflectivity spectrum of filter verses angle of incidence.....	4-8
Figure 4-4: Transmittance and phase verses angle of incidence	4-9
Figure 4-5: Transmission using the values of a and c	4-12
Figure 4-6: Transmittivity phase using the values of a and c	4-12
Figure 4-7: Calculated values of a and c for quarter wave structures.....	4-13
Figure 4-8: Reflection spectrum verses air gap thickness.....	4-14
Figure 4-9: Transmittance spectrum verses air gap size for $\lambda/4$ structure.....	4-15
Figure 5-1: Plots of pulses	5-2
Figure 5-2: Calculated reflectance spectra of a filter.....	5-4
Figure 5-3: Calculated reflectance spectra of a filter.....	5-6
Figure 5-4: Calculated reflectance spectra of a filter.....	5-7
Figure 5-5: Transmittance spectrum of a filter.....	5-10
Figure 5-6: Transmittivity spectrum of a filter	5-10
Figure 5-7: Transmittance spectrum of a filter.....	5-11
Figure 5-8: Transmittivity phase spectrum of a filter.....	5-11
Figure 5-9: Calculated reflectance spectrum and output pulse.....	5-13
Figure 5-10: Calculated reflectance spectrum and output pulse.....	5-14

Figure 5-11: Transmittance spectrum of a filter.....	5-16
Figure 5-12: Transmittivity phase spectrum of a filter.....	5-16
Figure 5-13: Calculated reflectance spectrum and output phase of a filter.....	5-17
Figure 5-14: Calculated transmittance and transmittivity phase.....	5-19
Figure 5-15: Spectrum difference between s and p polarized light.....	5-20
Figure 5-16: Output pulse.....	5-21

Abstract

The Air Force has a growing need for the greater bandwidth, speed, and flexibility offered by optical communication links. Future space systems and airborne platforms will most likely use optical signals for efficient power transmission and to minimize the possibility of spoofing and eavesdropping.

Tunable optical delays play an important role in the implementation of free space optical communication links. The primary challenge in implementing these systems is the active maintenance of coherent wave fronts across the system's optical aperture. For space applications, this aperture may be hundreds of meters in diameter. Spatial segmentation of a large aperture into smaller elements is one approach that can be used to solve the problem of coherent waveform maintenance.

In this research I explore three methods of achieving electrically tunable optical delay in a semiconductor structure. My first approach entails the use of multiple quantum wells inserted within the high index layers of a distributed Bragg reflector (DBR) to produce tunable optical delay when a transverse electric field is applied across the entire DBR. The second approach uses a cantilever mounted on top of a DBR structure. The cantilever is also a DBR and is used to vary the thickness of an air gap within the structure. A third approach relies on changing the angle of incidence of light on a DBR structure to produce a delay.

NUMERICAL STUDY OF OPTICAL DELAY IN SEMICONDUCTOR MULTILAYER DISTRIBUTED BRAGG REFLECTOR AND TUNABLE MICROCAVITY STRUCTURES

1.0 Introduction

1.1 Motivation

In this thesis I investigate the design and characterization of electrically controlled optical delay lines (ODL) composed of distributed Bragg reflectors (DBRs) containing absorbing multiple quantum well (MQW) layers. I also design and model electrically controlled ODLs constructed from DBR structures with a movable cantilever. Over the past decade, a significant body of work has been produced in the area of ODL. In fact, ODLs have become vital in improving and enhancing communications systems. Areas of importance include beam steering in free space optical interconnects, the generation of phased array coherent emitters, and switching networks. Furthermore, arrays of delay lines can be used in image correction to remove lens aberrations or adaptively correct for propagation of optical signals through turbulent media. Both military and commercial systems would benefit from improvements in tunable ODLs.

Optical systems provide many benefits over the more traditional microwave dishes or copper wire connections. Because optical systems support much higher frequencies than copper wires or microwave technology, they can be used to transmit much more data per second. Bandwidth is becoming more important for both commercial and military applications because the speed of transferring information in

many cases is the limiting factor in data processing. Optical systems also use relatively small components. This is a function of the smaller wavelength of the typical optical carrier. This is a huge advantage for space and air based systems because mass and size are very expensive commodities in payload bays.

Optical communication systems have greater signal to noise ratio than the other commercially available systems. This is because the frequency of electronic noise is too low to interfere with the photonic signal. Also the photon energy is much greater than the energy of an electron so electronic noise has very little effect on the signal. Finally, there is no cross talk in optical communication systems in contrast with electronic systems. This allows multiplexing with no signal loss due to carrier interaction. Hence, more bandwidth is available in optical systems.

The Air Force has a growing need for the greater bandwidth, speed, and flexibility offered by optical communication links. Future space systems and airborne platforms as shown in Figures 1-1 and 1-2, will most likely use optical signals for efficient power transmission and to minimize the possibility of spoofing and eavesdropping. Optical communication systems are difficult to intercept because they are line of sight systems.

Tunable optical delays play an important role in the implementation of free space optical communication links. The primary challenge in implementing these systems is the active maintenance of coherent wave fronts across the system's optical aperture [1]. For space applications, this aperture may be hundreds of meters in diameter. Spatial segmentation of a large aperture into smaller elements is one approach that can be used to solve the problem of coherent waveform maintenance. Each element can produce a

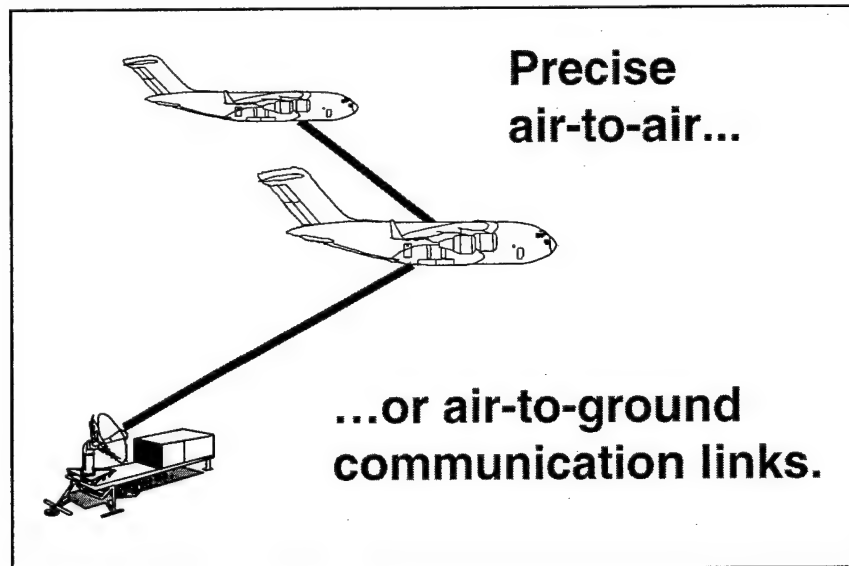


Figure1-1: Air-to-air and air-to-ground application of optical delay in free space communication

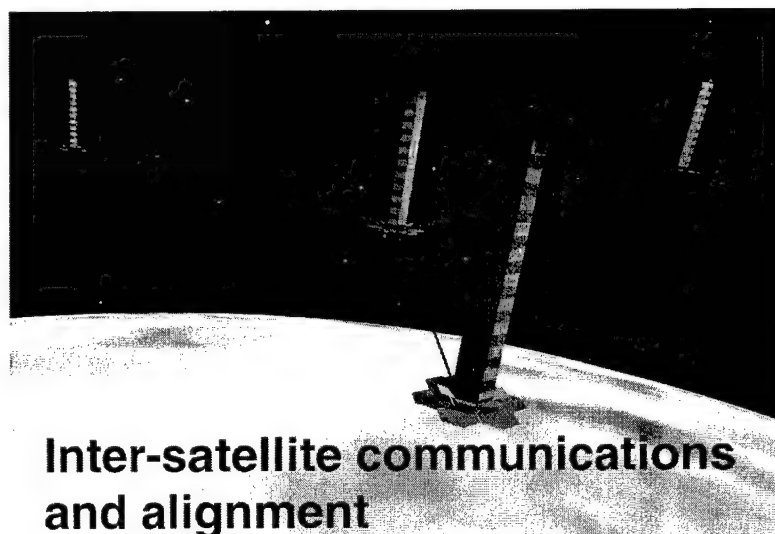


Figure 1-2: Space application of optical delay

correction for localized wave front phase errors. Together, all the elements maintain the coherence of the entire wave front [2].

1.2 Overview

Several approaches have been developed for the generation of tunable optical delays. Examples of these approaches include the use of piezo-electrically stretched optical fibers, transmissive and reflective liquid crystal spatial light modulators, and microlens or micromirror arrays. To characterize the method that is most appropriate for any given application, several design considerations must be taken into account. These include insertion loss, maximum achievable delay, drive current or voltage, speed of operation, wavelength of operation, bandwidth, and ease of integration into the given system. Hence, the application determines which method is best [1].

The basic idea of optical delay through a semiconductor element is shown in Figures 1-3 and 1-4. If a beam of light falls on an array of such elements, varying amounts of delay can be introduced into different parts of the beam by applying different electric fields across the different elements. If delay is implemented as shown in Figure 1-4, it is possible to deflect the beam without rotating the elements. This 'beam steering' has applications in space-based radar and free space interconnects.

In this research I explore three methods of achieving electrically tunable optical delay in a semiconductor structure. My first approach entails the use of MQWs inserted within the high index layers of a DBR to produce tunable optical delay when a transverse electric field is applied across the entire DBR. The second approach uses a cantilever mounted on top of a DBR structure. The cantilever is also a DBR and is used to vary the thickness of an air gap within the structure. A third approach relies on changing the

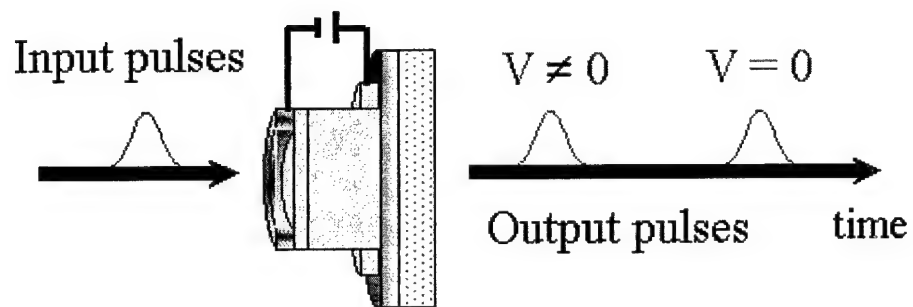


Figure 1-3: Schematic of a pulse delayed by a DBR structure with and without an electric field applied

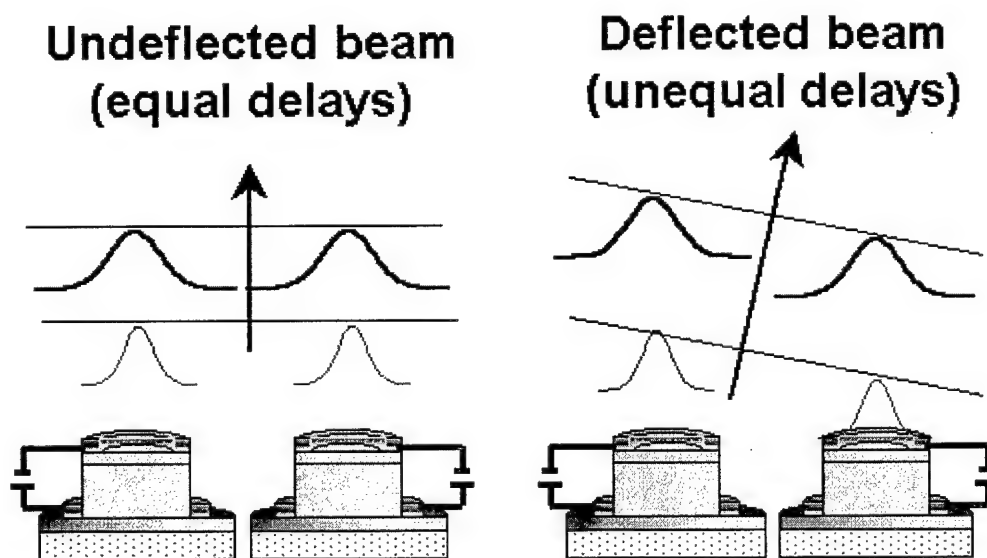


Figure 1-4: Schematic of beam steering implemented with unequal optical delay in a DBR array

angle of incidence of light on a DBR structure to produce a delay.

1.2.1 Field Induced Optical Delay in a DBR

The first structure proposed is a p-i-n MQW structure, which is reversed biased to produce an electric field across it as shown in Figures 1-5 and 1-6. The strength of the applied electric field changes the effective refractive index of the structure. The effective refractive index of the structure is related to the velocity of light in the medium by

$$v = c / n_{eff} \quad (\text{m/s}) \quad (1-1)$$

where v is the velocity of light in the medium, n_{eff} is the effective refractive index of the structure, and c is the speed of light in a vacuum. Let d equal the thickness of the structure and t the time taken for a pulse to propagate through the structure. If d/t is substituted for v in Equation 1-1, then

$$t = n_{eff} d / c \quad (\text{s}) \quad (1-2)$$

and

$$\Delta t = \Delta n_{eff} d / c \quad (\text{s}) \quad (1-3)$$

Hence changing the effective refractive index is one way an optical pulse can be delayed.

The use of electrically tunable DBR structures for optical delay has several advantages over other methods. First, these structures can be easily fabricated and integrated with vertical cavity surface emitting lasers (VCSELs). Also, no special alignment is necessary as the tunable structure may be grown directly on the VCSEL.

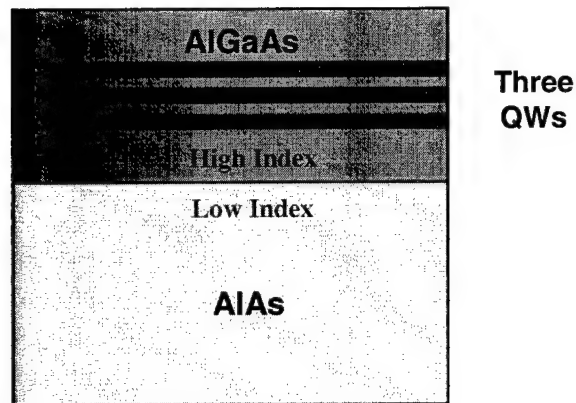


Figure 1-5: Single period of optical delay element containing 3QWs in the high index layer. Several of these periods are contained in the multi-period structure in Figure 1-6

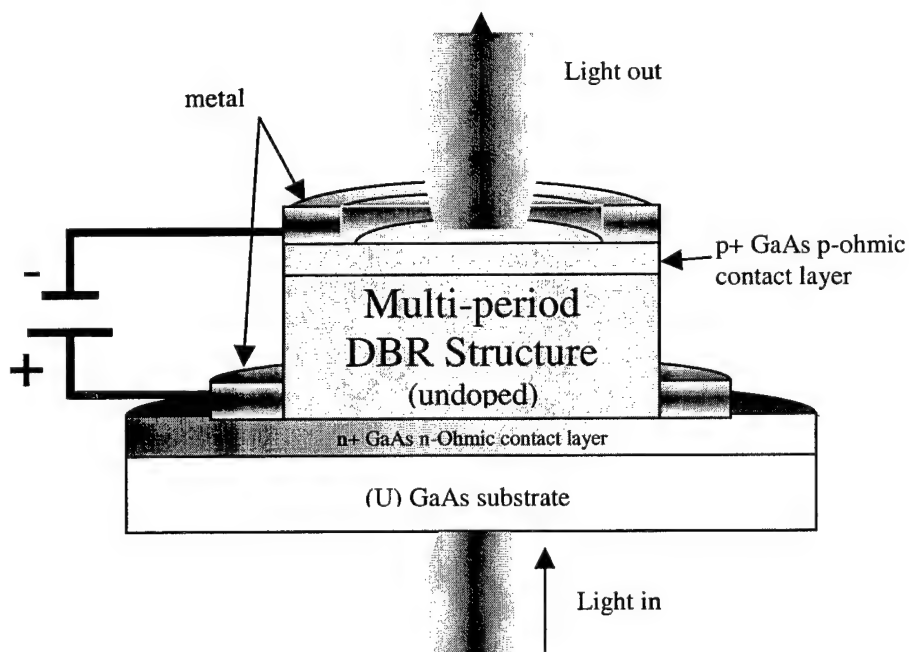


Figure 1-6: Schematic of complete p-i-n optical delay element under reverse bias.

Easy integration with VCSELs is important because VCSELs are the most likely optical sources for future communication networks. Further, the time scale inherent in this electrically switching method is very short (~ 1 ps), so that switching speeds are much faster than the other methods mentioned previously [1]. Finally, for spacebased and airborne applications the overall mass of the system should be as low as possible. The use of ODLs based on small DBR stacks ensures that the mass and size of the system is very small.

1.2.2 Variable Air Gap Tunable Optical Delay in a DBR

The second structure proposed for analysis is a variable air gap DBR structure as shown in Figure 1-7. These consist of one or more air gaps whose thickness can be varied by moving a cantilever DBR. Inducing an electrostatic force between the cantilever and the adjoining DBR(s) deflects the cantilever. To facilitate this, the layers on both sides of the air gap are heavily doped to allow the accumulation of charge when a voltage is applied.

From Equation 1-3, the optical delay in a DBR structure can be changed by varying the optical path length of the layers. The MQW device relies on changes in refractive index. In contrast, the tunable DBR seeks to change the physical thickness of one or more layers.

Lott [3] originally proposed this method as a means of producing tunable ODL. Currently, no literature exists on this subject. Similar structures have been constructed for other uses in silicon-based micro-electro-mechanical systems (MEMS). Fabrication remains an issue for a III-V compound semiconductor version of this MEMS-flexible ODL. The benefits of this MEMS device are similar to the benefits of MQW field

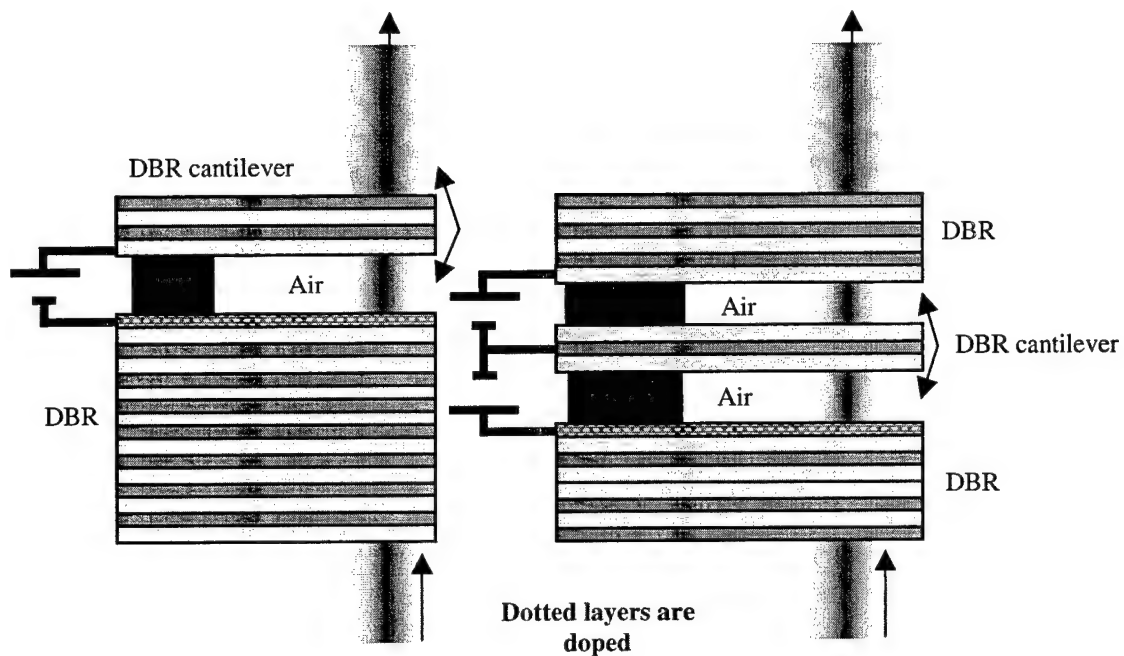


Figure 1-7: Single (left) and double (right) cantilever structures that are investigated to determine the changing optical delay with cantilever position. A potential difference applied across the various air gap(s) changes the thickness of these air gap(s) and thus the optical delay inherent in the structures.

induced delay device previously mentioned since commercial fabrication processes exist for these structures as well. The variable air gap structure integrates seamlessly with VCSEL technology, and is small and lightweight. The cantilever DBR structure can be designed to operate on low voltages for close integration with microelectronic circuits. Also, optically this structure is simple and it is easy to design similar delay elements that can operate in various frequency regions.

1.2.3 Variable Angle of Incidence Tunable Optical Delay in a DBR

The third method investigated in this thesis is the effect that changing the angle of incidence of incoming light has on the delay produced by the structure. Changing the angle of incidence of the light propagating through the structure causes the effective thickness of the structure to change. Equation 1-2 and 1-3 imply that changing the thickness of the layers will change the delay experienced by a pulse propagating through the structure.

Fabrication of this device is very similar to the previous two structures. However, currently no viable method is available for implementing this design in a practical system.

1.3 Scope

This thesis is solely a theoretical analysis of optical time delay through various DBR structures and does not include any experimental measurements. In this thesis I model reflectance, transmittance and transmittivity phase while changing different variables of the structures. For the MQW structure, the refractive index of some high layers is changed according to Feng's [4] data to simulate the application of an electric

field across the structure. In the variable air gap structure, the thickness of the air gaps are changed. In the variable angle of incidence structure, the angle of incidence is changed.

Simulations for the MQW structure are done for the $\text{Al}_{0.3}\text{Ga}_{0.7}\text{As}/\text{AlAs}$ material system. The design wavelength is near 810 nm. For both the variable air gap and variable angle of incidence structure, the material system is $\text{Al}_{0.1}\text{Ga}_{0.9}\text{As}/\text{AlAs}$ and the design wavelength is 1.55 μm . In all cases, the final structures are limited to quarter-wave layers and the substrate was assumed to be GaAs.

Finally, I develop a numerical time domain model that I use to propagate a Gaussian pulse of light through the DBR structures. This mathematical model allows me to calculate the optical delay experienced by a light pulse as it propagates through and exits individual multilayer structures.

1.4 Approach

The design and simulation of the electric field induced delay element is based on an $\text{Al}_{0.3}\text{Ga}_{0.7}\text{As}/\text{AlAs}$ DBR structure with quantum wells (QWs) composed of GaAs embedded in the $\text{Al}_{0.3}\text{Ga}_{0.7}\text{As}$ layers. The goal is to design a structure with high transmittance at a specific design wavelength that will give allow a high light pulse transmittance after an electric field is applied while changing the transmittivity phase in proportion to this applied field. My approach is to construct a multilayer bandpass filter with a wide nonabsorbing bandgap. I place absorbing QWs within the high index layers. The QW absorption varies with the applied electric field, and this in turn changes the structure's refractive index and thus it's transmittivity phase.

The variable air gap structure is composed of $\text{Al}_{0.1}\text{Ga}_{0.9}\text{As}/\text{AlAs}$ layers and one or two variable thickness air gap layers. My goal is to design a structure that maintains a high transmittance but a variable transmittivity phase when the thicknesses of the air gaps are changed. My designs are analyzed using a numerical model based on the standard 2x2 matrix method for multilayer optical structures.

My tilted structure is also composed of $\text{Al}_{0.1}\text{Ga}_{0.9}\text{As}/\text{AlAs}$ layers. When the structure is tilted, the effective optical thickness of the stack changes. This causes the transmittance and transmittivity phase to change. I designed the structure as a bandpass filter and changed the angle of incidence to simulate movement by electrostatic actuation.

The standard 2x2 transmission matrix method model is used to calculate the optical response of the devices to an optical input pulse propagated through the structure and substrate [5]. The model provides both transmittance and transmittivity phase information. For simplicity, the incident pulse is assumed to be Gaussian. Superimposed on this pulse is a narrow band of frequencies. The pulse is then multiplied with the transmittance of the structure in the frequency domain. The result is mathematically converted to the time domain to give the time delay of the pulse.

For the MQW structure the wavelength of interest is 807 nm. The wavelength of interest is 1.55 μm for the variable air gap structure and variable angle of incidence structure. I chose to simulate at 807 nm for the MQW structure simulations because this was the wavelength at which absorption is almost zero in the uncoupled well system presented by Feng and the refractive index change is still significant. This is illustrated in more detail in Chapter 2. I chose to simulate at 1.55 μm for the variable air gap and

variable angle of incidence structures because this wavelength has the lowest attenuation per unit length when propagating in conventional glass optical fibers.

1.5 Results

All the methods produced some theoretical measure of optical delay. The multiple quantum well structure produces more than 2π radians of delay when a 50kV/cm electric field is applied. This is achieved with little dispersion to the input pulse. Increasing the number of spacer regions and hence QWs in the structure can increase the optical delay. This will distort the input pulse more and uses a greater voltage to operate.

The two-cantilever variable air gap structure produces a maximum phase change of 2.63 radians when the cantilever is moved (together) through 380 nm. However, the transmittance of the structure ranges between 0.53 and 0.61 and significant dispersion occurs.

The variable angle structure produces more than 2π phase change when it is rotated through an angle of 0° to 40° . There is very little dispersion but pulse distortion occurs.

1.6 Summary

All the structures designed produces favorable results. The MQW structure produces the best results because there is a sizable change in phase of the structure with very little dispersion.

In Chapter 2 I present background information on the quantum confined Stark effect, optical filter design, the characteristic Matrix method of calculating reflectance transmittance and transmittivity phase and pulse delay.

In Chapter 3, I present my mathematical formulae and the models used in this theses. I describe how they are implemented and discuss their limitations.

In Chapter 4 I present the basic structures for the three methods of producing optical delay investigated in this thesis. The structures are developed from the models presented in Chapter 3.

In Chapter 5 I refine the structures developed in chapter 4 and analyze the performance of the structures.

Chapter 6 summarizes the research done in this thesis and proposes improvements which could be implemented and further research which can be undertaken.

References for Chapter 1

- [1] T. R. Nelson, J. P. Lochr, X. Qianghua, J. E. Ehret, J. E. Van Nostrand, L. Gamble, D. Jones, K., S. T. Cole, R. A. Trimm, W. Diffey, M., R. L. Fork, and A. S. Keys, "Electrically Tunable Group Delays Using Quantum Wells in a Distributed Bragg Reflector," *SPIE*, vol. 3714, pp. 12-23, 1999.
- [2] A. S. Keys and R. L. Fork, "Full Cycle, Low Loss, Low Distortion Phase Modulation from Multi-Layered Dielectric Stacks with Terahertz Optical Bandwidth," *Optical Society of America*, 1999.
- [3] J. A. Lott, Air Force Institute of Technology, Private Communication.
- [4] H. Feng, M. Sugiyama, K. Tada, and Y. Nakano, "Field Induced Optical Effect in a Five-Step Asymmetric Coupled Quantum Well with Modified Potential," *IEEE Journal of Quantum Electronics*, vol. 34, pp. 1197-1208, 1998.
- [5] W. H. Southwell, "Modeling Optical Thin Films," *Vacuum and Thinfilm*, 1999.

2.0 Background

2.1 Introduction

This chapter covers background information useful for an understanding of my numerical models and proposed device designs. This includes the design and analysis of multilayer distributed Bragg reflectors (DBRs), multilayer band pass filters, and aspects of optical delay calculations. I also discuss the quantum confined Stark effect (QCSE) and its effect on the refractive index of the material through the Kramers-Kronig relations.

2.2 DBR Structure

The typical DBR structure is a dielectric stack consisting of alternating layers of high refractive index and low refractive index material. Constructive interference of multiple reflections of light propagating through the structure generates very high reflectance, or, equivalently, very low transmittance over a range of wavelengths. This wavelength region is called the DBR transmission stopband. To either side of this region, interference produces a number of oscillations in the transmission spectra. The number of oscillations, their modulation depth, and the wavelength positions of the peaks and troughs are dependent upon the number of DBR layers, as well as the layer thicknesses and the dispersive indices of refraction of the constituent layers. Figure 2-1 shows a schematic of a MQW DBR comprised of alternating layers of high (H) and low (L) index layers. Each layer has an optical path length that is one-quarter of the stopband center

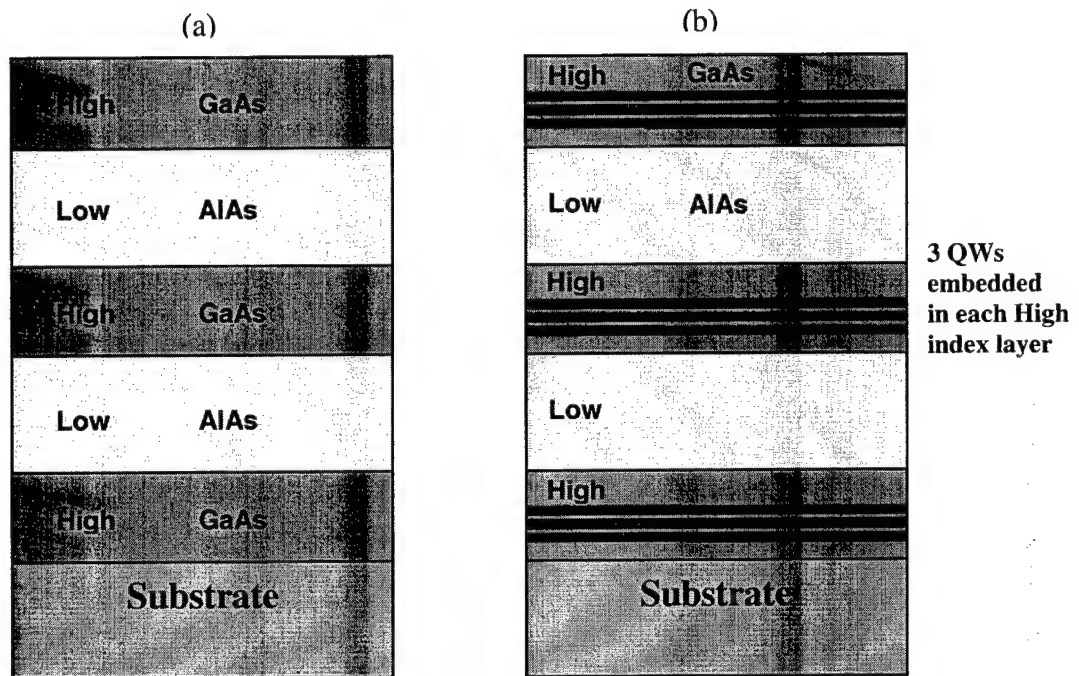


Figure 2-1: (a) Schematic of a typical DBR structure and (b) schematic of a DBR with three embedded quantum wells in each high index layer.

design wavelength. Figure 2-2 shows the calculated reflectance spectrum for 0 through 40-period DBRs comprised of alternating layers of $\text{Al}_{0.1}\text{Ga}_{0.9}\text{As}$ (high index) and AlAs (low index) layers on a GaAs substrate. The Bragg design wavelength was chosen to be 1063 nm. The first transmission peaks on either side of the DBR stopband are referred to as the short and long-wavelength band edge resonances, respectively. As Figure 2-2 shows, the band edges move based on the number of periods present in the DBR. Figure 2-3 shows the power reflectance and transmittivity phase of a 20-period DBR over the same range of frequencies.

2.3 Mirror Design Using the Characteristic Matrix Method

I used the characteristic matrix approach [1] to calculate the transmittance and transmittivity phase of the DBRs. This standard approach models the multiple reflections in the multi-layer medium as two additive optical fields within each layer; one traveling in the positive incident direction and the other in the negative or reflected direction. Figure 2-4 gives a visual description of this method. The positive going electric and magnetic field vectors in the m^{th} layer are denoted by E_m^+ and H_m^+ respectively. The reflected electric and magnetic field vectors in the m^{th} layer are denoted by E_m^- and H_m^- respectively. The total electric and magnetic fields in the m^{th} layer can then be written as

$$E_m = E_m^+ + E_m^- \quad (2-1)$$

$$H_m = H_m^+ + H_m^- = \mu_m (E_m^+ - E_m^-) \quad (2-2)$$

where μ_m is the effective refractive index of the m^{th} layer which may be complex if absorption is not zero. The values of μ_m are given by

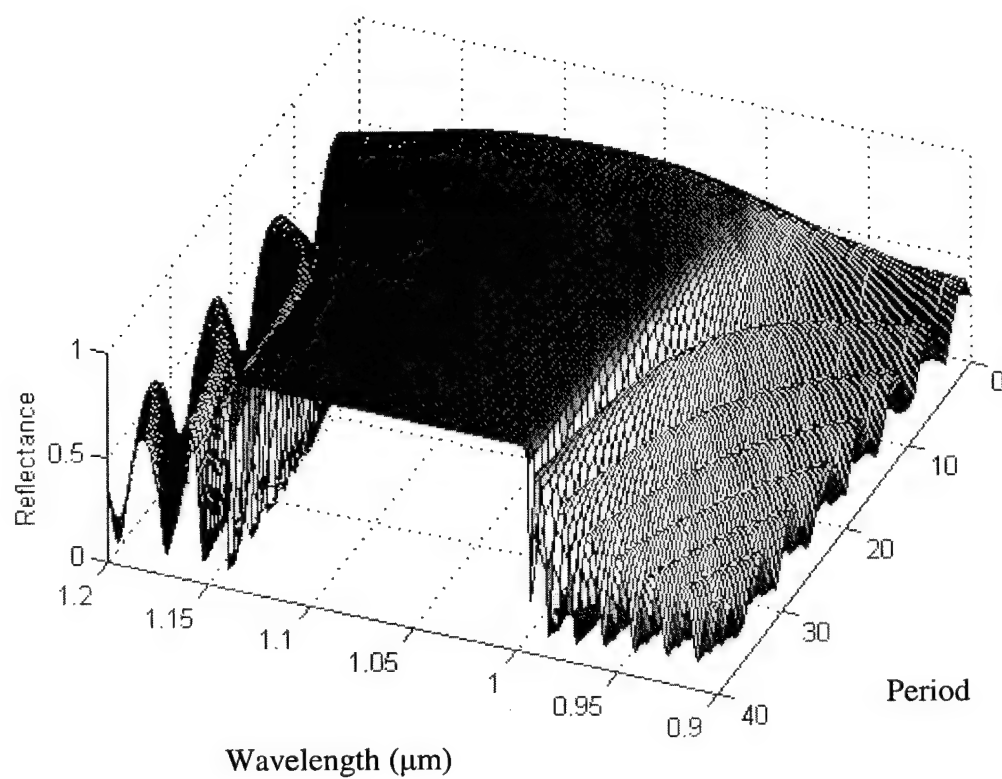


Figure 2-2: Calculated reflectance verses wavelength for 0 through 40 period DBRs using $\text{Al}_{0.1}\text{Ga}_{0.9}\text{As}/\text{AlAs}$ layers on a GaAs substrate. The central or Bragg wavelength is 1063 nm.

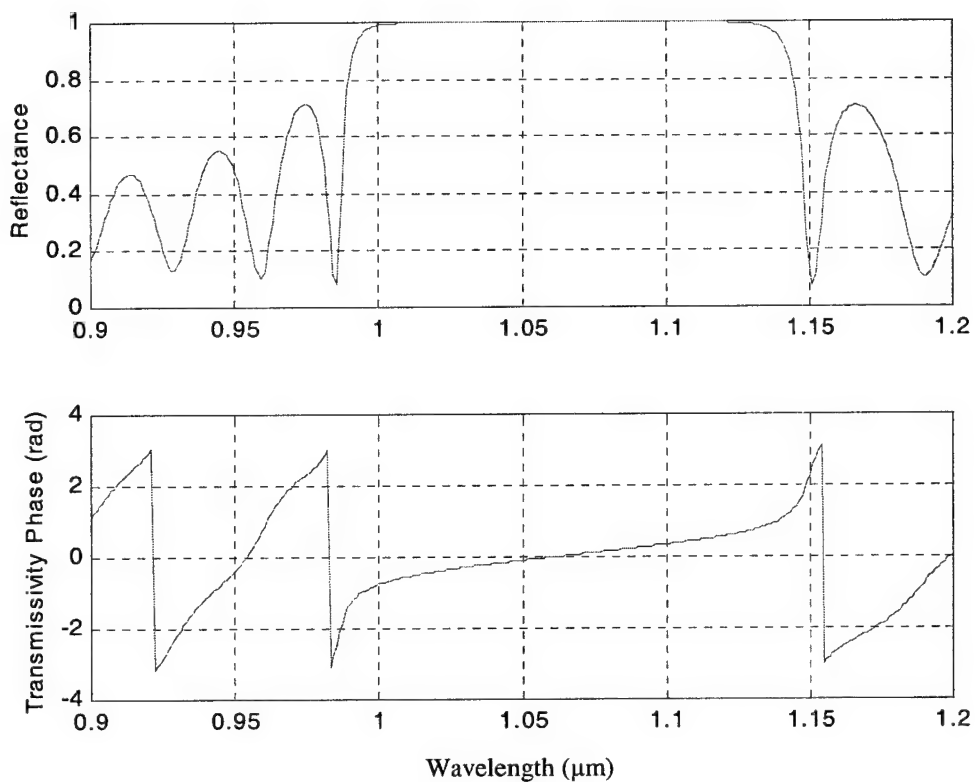


Figure 2-3: Calculated reflectance and reflectivity phase for a 20-period DBR composed of $\text{Al}_{0.1}\text{Ga}_{0.9}\text{As}/\text{AlAs}$ layers on a GaAs substrate. The Bragg wavelength is 1063 nm. Note the transmissivity phase equals 0 at the Bragg wavelength.

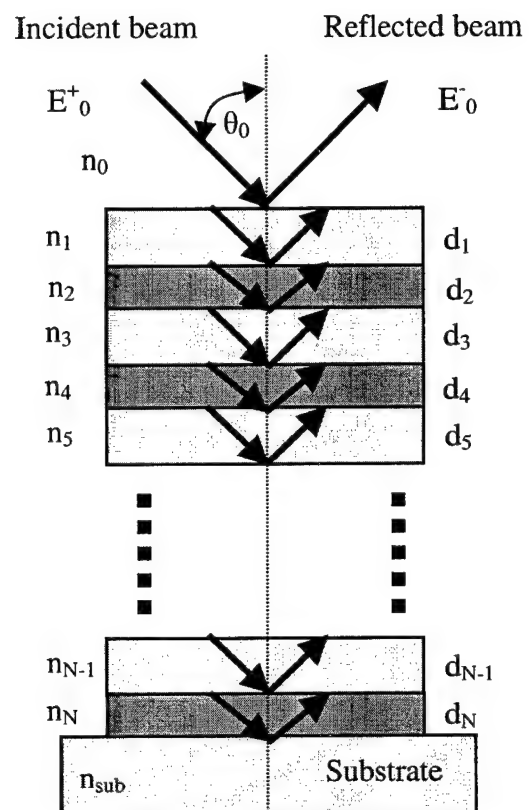


Figure 2-4: Geometry for reflected fields in a multilayer stack.

$$\mu_m = n_m / \cos \theta_m \quad \text{for the p polarization} \quad (2-3)$$

$$\mu_m = n_m \cos \theta_m \quad \text{for the s polarization} \quad (2-4)$$

where θ_m is the angle of incidence (off normal) of light in the m^{th} layer. This can be related to the external angle of incidence using

$$\cos(\theta_m) = \sqrt{(1 - (n_0 \sin \theta_0 / n_m)^2)} \quad (2-5)$$

The phase accumulated by a light phase front as it traverses the m^{th} layer is

$$\delta_m = \frac{2\pi n_m d_m \cos \theta_m}{\lambda_0} \quad (2-6)$$

where d_m is the physical thickness of the layer and λ_0 is the free space wavelength of the

light. For the case of normal incidence on a quarter wave layer at $\lambda_0 = \lambda_{\text{Bragg}}$, $d_m = \frac{u\lambda_0}{4}$,

where u is a positive integer, and thus

$$\delta_m = \frac{\pi \cos \theta_m}{2} \quad (2-7)$$

Using the matrix method developed by Heavens [1], I apply boundary conditions to the E and H fields incident at the interface. The solution of these boundary conditions is

$$\begin{bmatrix} E_{m-1}^+ \\ E_{m-1}^- \end{bmatrix} = \begin{bmatrix} \cos \delta_m & \frac{i}{\mu_m} \sin \delta_m \\ i\mu_m \sin \delta_m & \cos \delta_m \end{bmatrix} \begin{bmatrix} E_m^+ \\ E_m^- \end{bmatrix} \quad (2-8)$$

I can easily extend the single layer solution to an N-layer stack by writing

$$\begin{bmatrix} E_0 \\ H_0 \end{bmatrix} = \prod_{m=1}^N M_m \begin{bmatrix} E_N \\ H_N \end{bmatrix} \quad (2-9)$$

where E_0 and H_0 are the incident electric and magnetic fields and M_m is the Characteristic Matrix, given by

$$M_m = \begin{bmatrix} \cos \delta_m & \frac{i}{\mu_m} \sin \delta_m \\ i\mu_m \sin \delta_m & \cos \delta_m \end{bmatrix} \quad (2-10)$$

I can then determine the field exiting the multi-layer stack via the substrate by using

$$\begin{bmatrix} E_0 \\ H_0 \end{bmatrix} = \prod_{m=1}^{N+sub} M_m \begin{bmatrix} E_{sub} \\ H_{sub} \end{bmatrix} = \prod_{m=1}^{N+sub} M_m \begin{bmatrix} 1 \\ \mu_{sub} \end{bmatrix} E_{sub} \quad (2-11)$$

If only a normal angle of incidence and $\lambda/4$ layer thicknesses are considered, then at the design wavelength

$$M_m = \begin{bmatrix} 0 & \frac{i}{\mu_m} \\ i\mu_m & 0 \end{bmatrix} \quad (2-12)$$

and thus

$$\begin{bmatrix} E_0 \\ H_0 \end{bmatrix} = \prod_{m=1}^{N+sub} \begin{bmatrix} 0 & \frac{i}{\mu_m} \\ i\mu_m & 0 \end{bmatrix} \begin{bmatrix} 1 \\ \mu_{sub} \end{bmatrix} E_{sub} \quad (2-13)$$

From the resulting matrix on the left of the equality in Equation 2-13, power reflectance R , transmittivity t , and power transmittance T can be found directly [2] as

$$R = \left(\frac{E_0 \mu_0 - H_0}{E_0 \mu_0 + H_0} \right)^2 = r^2 \quad (2-14)$$

$$t = \frac{2\mu_0}{E_0 \mu_0 + H_0} \quad (2-15)$$

and

$$T = \frac{\mu_{sub} |t|^2}{\mu_0} \quad (2-16)$$

The absorption A is then calculated by using

$$R + T + A = 1 \quad (2-17)$$

2.3.1 Band Pass Filter Design

There are several methods that can be used to design multilayer band pass filters. The method I used is to cascade several Fabry-Perot filters to give an extended region of high transmittance [1]. Each Fabry-Perot filter consists of a reflector (DBR) at a fixed wavelength. The number of reflectors determines the width of the pass band while the number of periods in each reflector determines the steepness and rejection in the stop band. The basic Fabry-Perot filter design looks like the following:

incident medium | DBR reflector | halfwave layer | DBR reflector | substrate medium
where a halfwave represents an integer multiple of $\lambda/2$ -thick spacer layer. The following equations describe the transmittance $T(\lambda)$ seen by a photon from within the spacer layer as it propagates towards the top and bottom DBR [1].

$$T(\lambda) = T_0(\lambda) \frac{1}{1 + F(\lambda) \sin^2 \left[\frac{(\varphi_1 + \varphi_2)}{2} - \delta \right]} \quad (2-18)$$

$$T_0(\lambda) = \frac{(1 - R_1) \cdot (1 - R_2)}{(1 - \sqrt{R_1 R_2})^2} \quad (2-19)$$

$$F(\lambda) = \frac{4\sqrt{R_1 R_2}}{(1 - \sqrt{R_1 R_2})^2} \quad (2-20)$$

where R_1, R_2, ϕ_1 and ϕ_2 are the reflectance and reflectivity phase respectively of the top and bottom mirrors as seen from within the microcavity and $\delta = 2\pi nd / \lambda$ is the optical thickness of the microcavity.

The transmittance of the filter is low in the passband because of the sharp change in refractive index that exists between the structure and the incident and substrate material. Several methods can be used to minimize this. However, I use Thelen's method [1] to ensure impedance matching of the structure and the incident and substrate layers. This involves placing an additional admittance matched interface between the structure and the external layer. This interface is made up of quarter-wave layers and has an admittance that falls between the external layer and the structure. This greatly improves the performance of the filter in the pass band.

2.4 Group and Phase Velocity in a DBR

Optical pulse delay in DBR structures was previously considered by Dowling, Scalora, and co-workers [3]. Theoretically, they predicted that optical pulses incident at the transmission bandedge resonances experience a group delay that is proportional to the square of the number of DBR periods. Their initial treatment was based on a transfer-matrix calculation of the complex transmission coefficient. They showed that the group velocity,

$$v_{group} \equiv \frac{d\omega}{d\kappa} \quad (\text{m/s}) \quad (2-21)$$

where ω is the angular velocity and κ is the wave number, scales inversely with the derivative of the transmittivity phase, ϕ , with respect to optical frequency, such that

$$Delay \propto \frac{1}{v_{group}} = \frac{dk}{d\omega} \propto \left| \frac{d\phi}{d\omega} \right| \quad (s) \quad (2-22)$$

Hence, in regions where the slope of the transmittivity phase is large, the group velocity for an incident pulse becomes very small, and the delay experienced by the pulse traveling through the structure is large. Scalora verified these findings experimentally in 1996 [4]. Optical pulse delays of 0.27 ps were found for a 30-period GaAs/AlAs DBR, with negligible distortion of 2 ps laser pulses. Good agreement to the measurements was obtained using both transfer-matrix (frequency domain) and pulse propagation (time domain) simulations [4, 5].

It must be emphasized that a fixed DBR structure alone provides only a static group delay. To provide tunability, some means of changing the optical path length (and hence the transmittivity phase) of the structure must be introduced. This can be evaluated by considering the phase velocity v_{phase} of the structure

$$v_{phase} = \frac{\omega}{\kappa} = \frac{\Delta\phi}{\Delta t} \cdot \frac{\lambda}{n_{eff}} \cdot \frac{1}{2\pi} \quad (rad \frac{m}{s^2}) \quad (2-23)$$

where $\Delta\phi$ is interpreted with respect to λ as the absolute change in phase accumulation within time Δt . The average effect of the refractive index in the dielectric stack through which the wave front propagates is n_{eff} . If the path length traversed by the propagating wave front is defined to be Δd , then $\frac{\Delta d}{v_{phase}}$ can be substituted for Δt . By manipulating

Equation 2-22, I find the change in phase of the propagating pulse in terms of the structure's effective refractive index and path length to be

$$\Delta\phi = \frac{2\pi\Delta d n_{eff}}{\lambda} \quad (rad) \quad (2-24)$$

Modulation of either d or n_{eff} will result in modulation of the signal's phase. Changing the angle of incidence provides one way to change d while applying an electric field across the MQW DBR structure will change n_{eff} .

From Equation 2-21, $v_{group} = \frac{d\omega}{dk}$. Using Equation 2-23, the fact that $k = \frac{2\pi}{\lambda}$, and $dk = \left(-2\pi/\lambda^2\right)d\lambda$, the group velocity becomes

$$v_{group} = \left(v_{phase}\right) - \lambda \left(\frac{d\left(v_{phase}\right)}{d\lambda} \right) \quad (\text{m/s}) \quad (2-25)$$

Hence, maximizing the rate at which the transmitted signal phase changes with respect to wavelength minimizes the group velocity and maximizes the optical pulse delay. This creates not only a desirable region for phase modulation, but also a mechanism for introducing a known amount of group delay to the transmitted signal [6].

2.5 Excitonic Transitions and Absorption

2.5.1 Bulk Material

In a very pure undoped bulk semiconductor, electrons and holes produced by absorption of a photon of near-band gap energy pair to form an exciton [7]. The optical exciton usually is seen as a series of sharp resonance peaks at the low energy side of the band edge in the absorption spectra of direct band gap semiconductors. The total energy of the exciton is

$$\epsilon_{ex} = \frac{\hbar^2 k_{ex}^2}{2\left(m_e^* - m_h^*\right)} - \frac{-13.6 m_r^*}{l^2 m_o e_r} \quad l=1, 2, 3, \dots \quad (\text{eV}) \quad (2-25)$$

where k_{ex} is the momentum of the exciton, $m_{e(h)}^*$ is the electron (hole) effective mass, \hbar is the reduced Planck's constant, and m_0 and m_r^* are the electron rest mass and the reduced effective mass, respectively. The first term is the kinetic energy of the exciton. For direct semiconductors $k_{ex} \cong 0$ because the electron and hole must move in the same direction [7]. Because of the excitonic binding energy, the absorption transitional energy red shifts. This is expressed as

$$\hbar\omega = \varepsilon_g \pm \varepsilon_p - \varepsilon_{ex} \quad (\text{eV}) \quad (2-26)$$

where ε_p is the photon energy absorbed or emitted, ε_g is the energy gap, and ε_{ex} is the excitonic energy. Figure 2-5 shows the process of excitonic absorption in pure GaAs at various temperatures. The excitonic energy becomes more pronounced at colder temperatures [7]. The excitonic transition's position and size is sensitive to electric field strength. Hence I can control absorption and refractive index by applying a voltage, which changes the energy of the excitonic transitions.

2.5.2 Uncoupled Quantum Wells

In uncoupled MQWs (i.e. the barrier layer is wide enough so that the electron or hole wavefunctions do not interact) the excitonic effects are much greater than in bulk material. Electrons and holes and hence the wavefunctions are confined in a region defined by the well width. Hence, the electron and hole wavefunction overlap is increased as shown Figure 2-6. This results in a greater oscillator strength of the

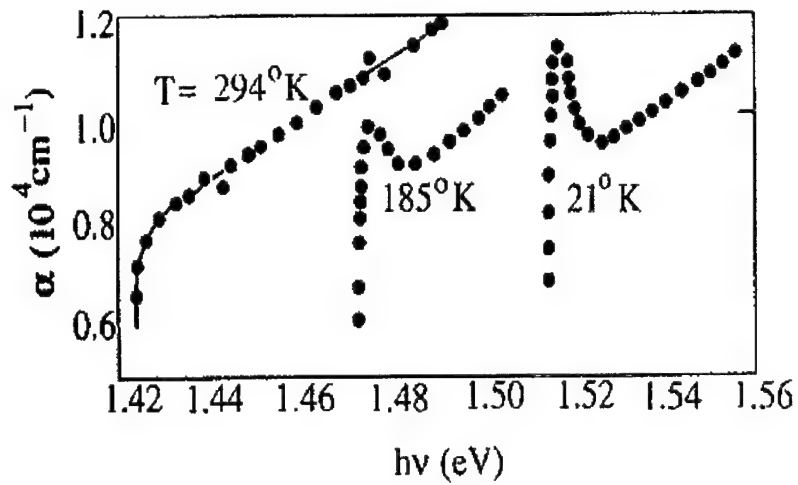


Figure 2-5: Absorption coefficient measured near the band edge of bulk GaAs at $T=294$ K, 185 K and 21 K. The two absorption peaks at $h\nu$ slightly below the respective band gap at 185 K and 21 K are due to bound excitons [7].

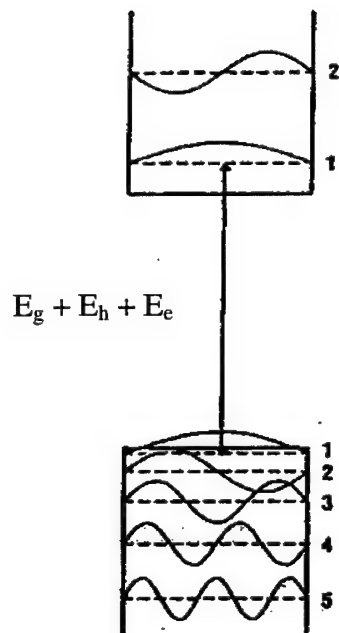


Figure 2-6: Schematic of a QW energy diagram with energy levels and wave functions depicted where E_g is the energy gap, E_h is the hole energy level and E_e is the electron energy level [8].

interband transition between the discrete electron and hole energy bound states. Because of this, strong resonances corresponding to heavy-hole and light-hole transitions are seen near the band edge even at room temperature. Figure 2-7 shows the calculated absorption spectra of an $\text{In}_{0.53}\text{Ga}_{0.47}\text{As}$ (100Å)/ $\text{In}_{0.52}\text{Al}_{0.48}\text{As}$ (100Å) MQW structure lattice matched to InP [7]. The resonance for the e1-hh1 can be clearly seen corresponding to the excitonic absorption in the well at about 1605 nm. This absorption peak is not visible in bulk InGaAs material. For a purely two-dimensional exciton, the binding energy has been calculated to be four times higher than in the bulk case. However, because of the extensions of the wavefunctions into the barrier, the binding energy in practical QWs range from $2 \epsilon_{\text{ex}}$ to $3 \epsilon_{\text{ex}}$, where ϵ_{ex} is the binding energy in bulk material [7].

2.5.3 Coupled Asymmetric Quantum Wells

If the QW's are coupled, (less than 100 Å barrier material [9]), the interactions of the wavefunctions become more complicated and are not easy to analyze. However, work by Feng [10] indicates that greater changes in absorption can be achieved with coupled asymmetric systems at much lower reverse bias than previously measured using uncoupled MQW. I described Feng's results in Section 2.8.

2.6 Quantum Confined Stark Effect (QCSE)

When a transverse electric field is applied to a MQW structure, an induced birefringence occurs which is manifested by a change in the refractive index of the structure in both the directions of the ordinary and extraordinary rays [7]. This is depicted

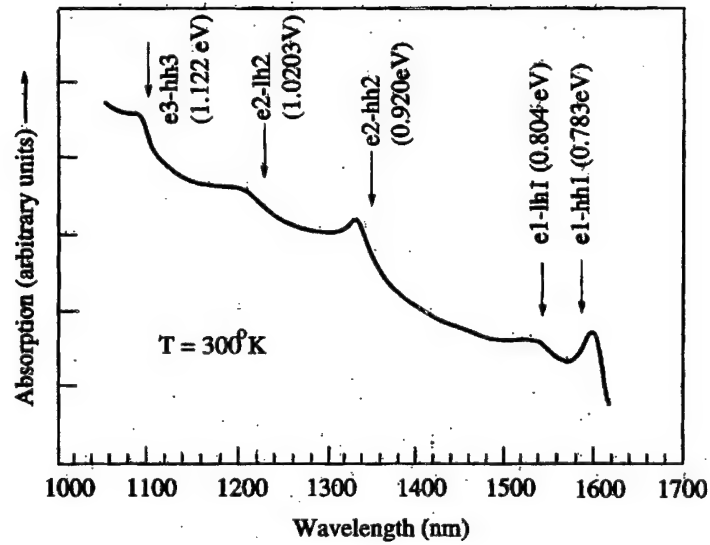


Figure 2-7: The calculated transitions based on a finite square well model at 300°K for an $\text{In}_{0.53}\text{Ga}_{0.47}\text{As}$ (100Å)/ $\text{In}_{0.52}\text{Al}_{0.48}\text{As}$ (100Å) MQW structure lattice matched to InP. The parameters e1, e2 and e3 are the first, second and third electron energy levels respectively. The parameters hh1, hh2 and hh3 are the first, second and third heavy hole energy levels respectively. The parameter lh1 is the light hole energy level [7].

in the energy band diagram by a separation of the electron and hole wavefunction as they are pushed towards the opposite sides of the well [8, 11], as shown in Figure 2-8. This results in a reduction in overlap of the wavefunctions, which is seen as a decrease in absorption, luminescence peaks, and broadening of the absorption linewidth. The energy bands also become tilted. This phenomenon produces a red shift in resonance, which increases with increasing electric field. This shift is quadratically dependent on the applied electric field [7]. The transitional energy of a QW structure under an electric field is given by

$$\hbar\omega = \varepsilon_g \pm \varepsilon_p + \varepsilon_c + \varepsilon_v - 2\varepsilon_{ex} \quad (\text{eV}) \quad (2-27)$$

Figure 2-9 indicates the experimental variation of absorption with electric field for an AlAs/GaAs DBR. Changes to the exciton absorption and transition energies naturally give rise to changes in refractive index via the Kramers-Kronig relations [11].

2.7 The Kramers-Kronig Relations

The QCSE has an impact absorption and hence on the refractive index of the MQW structure. Let the refractive index of the structure be given by

$$n = n_r + i\kappa_a \quad (\text{unitless}) \quad (2-28)$$

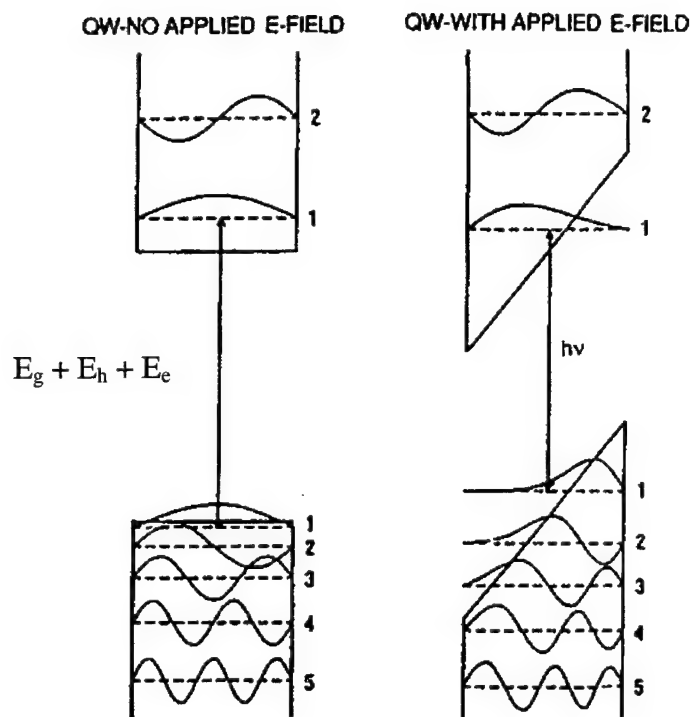


Figure 2-8: Demonstration of effects of electric field on wavefunction and band energies of a QW [8]. The transition energy is reduced and the wave function overlap decreases as the electric field increases.

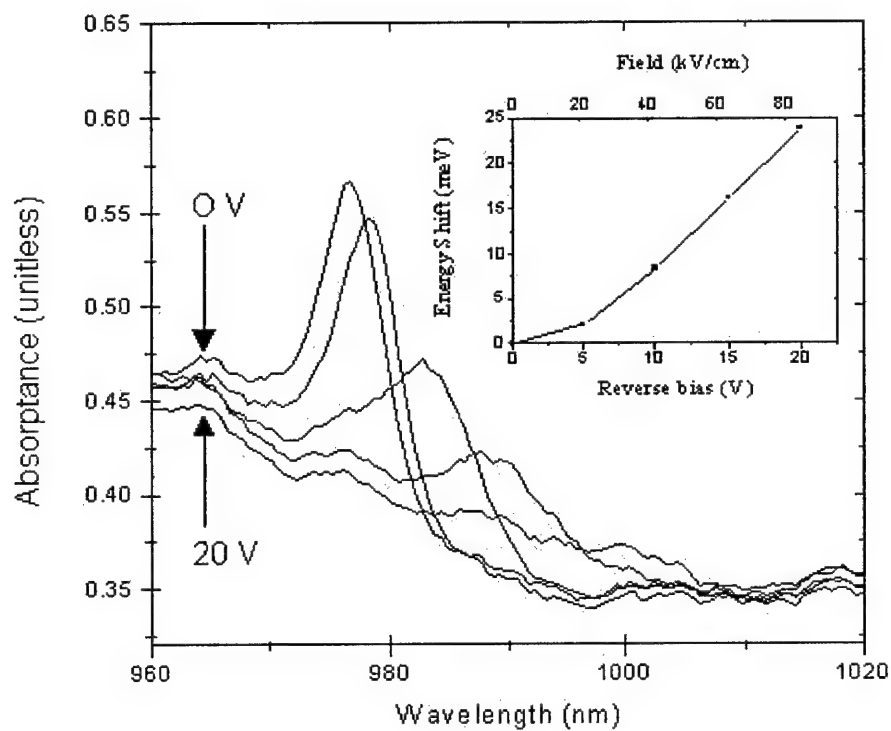


Figure 2-9: Electric field dependence of absorbance under various voltage biases for 12 80Å $\text{In}_{0.2}\text{Ga}_{0.8}\text{As}/\text{GaAs}$ QW separated by 1000Å GaAs barrier. As the voltage is increased from 0V to 20V the peaks on the plots diminish. The insert shows the red shift in absorption peak energy experienced when an increasing electric field is applied.[5].

where n_r and κ_a are the real and imaginary parts of n . Since the imaginary part is a measure of the loss in power of a wave propagating through the layer, $\kappa_a \propto \alpha$, where α is the absorption coefficient of the semiconductor layer. Given a plane wave described by

$$E = E_0 \exp\left[j\alpha\left(\frac{x}{v} - t\right)\right] = E_0 \exp\left[j\omega\frac{n_r x}{c} - t\right] \exp\left(-\frac{\omega\kappa_a x}{c}\right) \quad (\text{V/m}) \quad (2-29)$$

where E_0 is the amplitude of the wave is propagating in the positive x direction with velocity $v = c/n$, then

$$\alpha = \frac{2\omega\kappa_a}{c} \quad (\text{cm}^{-1}) \quad (2-30)$$

In a material whose conductivity $\sigma \rightarrow 0$, the refractive index is related to the dielectric constant by the relation

$$n_r \cong \sqrt{\epsilon_r} \quad (2-31)$$

where ϵ_r is the static dielectric constant and $\kappa_a \cong 0$.

It has been demonstrated that

$$\Delta n_r(\epsilon) = \frac{ch}{2\pi^2} P \int_0^\infty \frac{\Delta\alpha(\epsilon')}{\epsilon'^2 - \epsilon^2} d\epsilon' \quad (\text{unitless}) \quad (2-32)$$

where ϵ to ϵ' is the energy window over which the integration is performed, P is the principal value for the Cauchy integral, and $\Delta\alpha$ is the change in the absorption coefficient. It can be deduced that the refractive index is inversely related to the band gap of the material and proportional to the absorption coefficient [7]. This is a form of the Kramers-Kronig relations. Applying an electric field across an MQW structure

changes both the band gap and the absorption coefficient as described by the QCSE. This in turn changes the refractive index and hence the optical properties of the structure.

2.8 Optimal Quantum Well Structure

I am interested in maximizing both the rate of change of refractive index with electric field and the absolute magnitude of change in refractive index. To do this I considered Equation 2-32, which show how changes in the absorption coefficient affect the change in refractive index. The equation is an integral over the region where absorption has changed when a field is applied. So, if the change in the absorption coefficient changes sign, it adversely affects the rate of change and the absolute change of refractive index [12]. This is because integrating past the point where the coefficient changes sign essentially is a subtraction from the change in refractive index. Figure 2-10 is a schematic that shows the two possible groups of absorption spectra change, which can be expected in QW structures when a transverse electric field is applied [10]. The spectrum in Figure 2-10(a) gives a smaller change in refractive index than those in Figure 2-10(b) at wavelengths longer than the band edge. Uncoupled QWs generally give changes in absorption coefficients similar to those shown in Figure 2-10(a) [12]. Figure 2-11 shows a five step asymmetric coupled QW (FACQW) structure developed by Feng [10]. The change in absorption spectra and refractive index is shown in Figures 2-12 and 2-13 for a rectangular QW (RQW) and a FACQW [10]. The RQW is a 35 monolayer (ML) GaAs well with $\text{Al}_{0.3}\text{Ga}_{0.7}\text{As}$ barriers on either side [10]. The change in refractive index is orders of magnitude greater for the FACQW than the RQW.

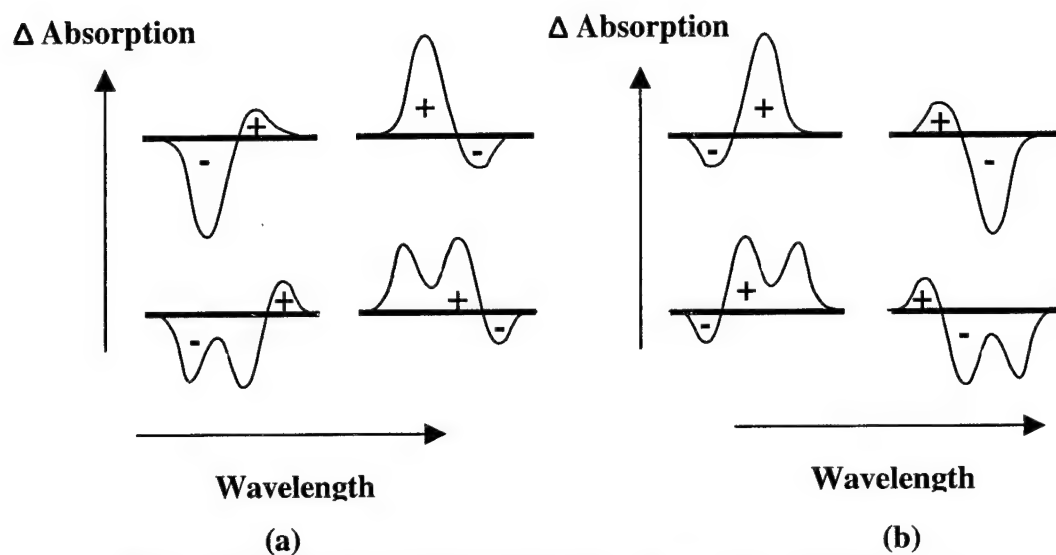


Figure 2-10: Schematic of possible absorption change with wavelength. (a) leads to the least change in refractive index while (b) leads to the greatest change at wavelengths away from the absorption edge [10].

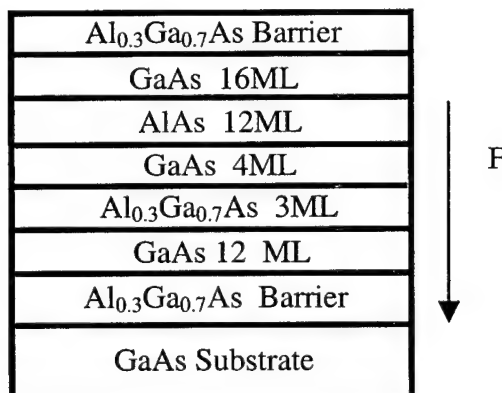


Figure 2-11: Schematic layer structure of the five step asymmetric coupled QW. A monolayer (ML) is 2.83 Å [10].

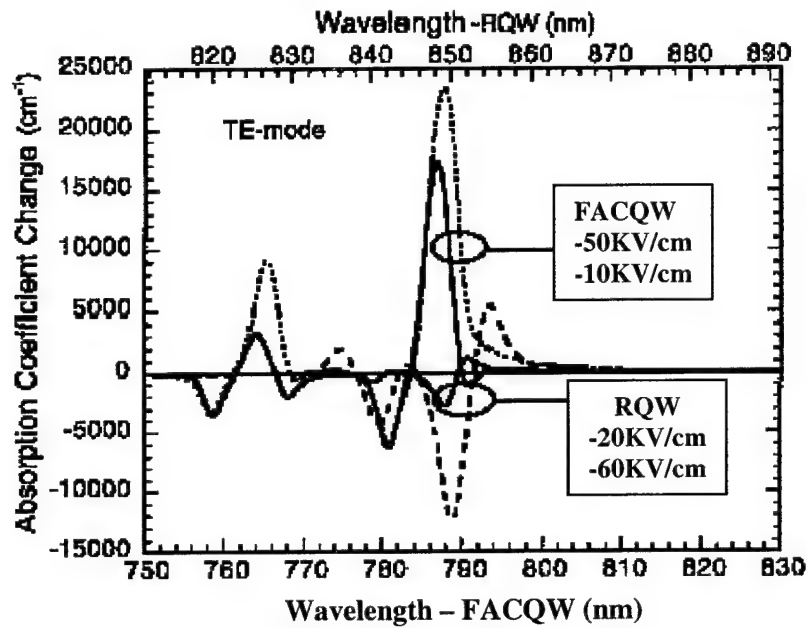


Figure 2-12: Absorption coefficient change for a rectangular QW and a five step asymmetric coupled QW under various electric fields compared to a zero applied bias [10].

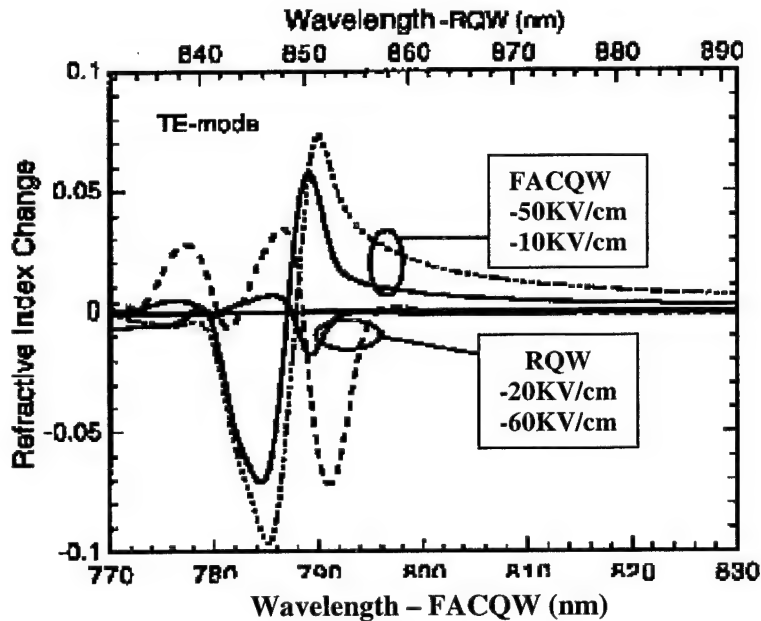


Figure 2-13: Refractive index change for the structures in Figure 2-12 compared to a zero applied bias [10].

2.9 Optical Delay Calculations

When a pulse propagates through one of the DBR structures, the output pulses that emerge will be delayed, compared to propagation through air. However, the optical delay changes when an electric field is applied in the MQW structure, the air-gap is varied in the variable air-gap DBR structure, or the DBR structure is tilted.

I use a frequency-based analysis to simulate the delay in my DBR structures. I use the characteristic matrix method to calculate the transmittance of the DBR for an optical pulse that is propagating through the structure [2].

The pulse used in the simulation is chosen to be a Gaussian function in time as

$$E_{in}(t) = Ae^{\frac{-(t-t_0)^2}{2\sigma^2}} e^{j\omega_0 t} \quad (2-33)$$

where ω_0 is the angular frequency, t_0 is the point in time when the pulse originates and σ is $\sqrt{2 \ln 2}$ times the full width at half maximum (FWHM) of the pulse. The parameter A is the amplitude of the pulse.

The Fourier Transform (FT) of the input pulse is taken. Theoretically the FT and inverse FT are of the form [13]

$$E_{in}(\omega) = 2\pi \int_{-\infty}^{\infty} E_{in}(t) e^{-j\omega t} dt \quad (3-34)$$

and

$$E_{in}(t) = \frac{1}{2\pi} \int_{-\infty}^{\infty} E_{in}(\omega) e^{j\omega t} d\omega \quad (2-35)$$

where ω and t represent frequency and time respectively. The transformed pulse $E_{in}(\omega)$ is then multiplied with the transmittance of the structure $T(\omega)$. The result is then converted to the time domain using Equation 2-35. The result is an expression for the delayed optical pulse.

The Fourier transform analysis predicts that a change in the transmittivity phase of a pulse in the frequency domain causes the pulse to time-shift in the time domain. If the phase change is linear, the pulse shape is preserved. However, a non-linear phase change leads to distortion of the pulse as various pulse components are delayed by different amounts [13]. To prevent distortion, the phase change must be linear within the FWHM of the pulse in the frequency domain.

If the transmittivity phase change is linear, then the optical pulse delay is equal to $(\Delta\phi/2\pi)T_0$ where $\Delta\phi$ is the phase change, and T_0 is the period of the central wavelength (λ_0).

2.10 Summary

This chapter described various DBRs including Fabry Perot etalon structures and their optical properties. The characteristic Matrix method which is used to calculate reflectance, transmittance and transmittivity phase in DBR's was described.

The QCSE was discussed for both coupled and uncoupled quantum wells and it's relationship to change in refractive index under various electric field strengths. It was found that the QCSE was much stronger in coupled wells with a specific type of absorption spectrum than uncoupled wells.

The group velocity for an optical pulse was found to be proportional to the slope of the transmittivity phase in a DBR. Hence, maximizing the rate of change of phase with wavelength maximizes the group delay of the structure.

The background presented in this chapter will be used in Chapter 3 to develop transmittance, reflectance and time delay model for analyze various DBR structures.

References for Chapter 2

- [1] H. A. Macleod, *Thin-Film Optical Filters*, 2nd ed: Macmillan Publishing Company, 1986.
- [2] W. H. Southwell, "Modeling Optical Thin Films," *Vacuum and Thinfilm*, 1999.
- [3] J. M. Bendickson and J. P. Dowling, "Analytic Expressions for the Electromagnetic Mode Density in Finite, One-Dimensional, Photonic Band-Gap Structures," *Physical Review E*, vol. 53, pp. 4107-4121, 1996.
- [4] J. M. Scalora, J. M. Bendickson, J. P. Dowling, and R. L. Fork, "Ultrashort Pulse Propagation at the Photonic Band Edge: Large Tunable Group Delay with Minimal Distortion," *Physical Review*, vol. E54, pp. R1078-R1081, 1996.
- [5] T. R. Nelson, J. P. Loehr, X. Qianghua, J. E. Ehret, J. E. Van Nostrand, L. Gamble, D. K. Jones, S. T. Cole, R. A. Trimm, W. M. Diffey, R. L. Fork, and A. S. Keys, "Electrically Tunable Group Delays Using Quantum Wells in a Distributed Bragg Reflector," *SPIE*, vol. 3714, pp. 12-23, 1999.
- [6] A. S. Keys and R. L. Fork, "Full Cycle, Low Loss, Low Distortion Phase Modulation from Multi-Layered Dielectric Stacks with Terahertz Optical Bandwidth," *Optical Society of America*, 1999.
- [7] P. Bhattacharya, *Semiconductor Optoelectronic Devices*, 2nd ed. Upper Saddle River, NJ: Prentice Hall, 1997.
- [8] C. Weisbuch and B. Vinter, *Quantum Semiconductor Structures*. San Diego: Academic Press, Inc., 1991.

- [9] R. J. Bagnell, "Design and Characterization of Optically Pumped Vertical Cavity Emitting Lasers," Thesis in *Electrical Engineering*. Dayton: Air Force Institute of Technology, 1992.
- [10] H. Feng, M. Sugiyama, K. Tada, and Y. Nakano, "Field Induced Optical Effect in a Five-Step Asymmetric Coupled Quantum Well with Modified Potential," *IEEE Journal of Quantum Electronics*, vol. 34, pp. 1197-1208, 1998.
- [11] Y. Kan, H. Nagai, and M. Yamanishi, "Field Effects on the Refractive Index and Absorption Coefficient in AlGaAs Quantum Well Structures and Their Feasibility for Electrooptic Device Applications," *Journal of Quantum Electronics*, vol. QE-23, 1987.
- [12] N. Susa, "Electric-Field-Induced Refractive Index Change in Three-Step Asymmetric Coupled Quantum Wells," *Journal of Applied Physics*, vol. 73, pp. 8463-8470, 1993.
- [13] A. V. Oppenheim, A. S. Willsky, and H. S. Nawab, *Signals and Systems*, 2nd ed. New Jersey: Prentice Hall, 1997.

3.0 Modeling

3.1 Introduction

In this chapter I present the models I developed for this thesis. I modeled several device parameters including the index of refraction of $\text{Al}_x\text{Ga}_{1-x}\text{As}$ from 400 nm to 1700 nm, power reflectance and transmittance, transmittivity phase, and optical pulse delay calculations. My models allow changes of refractive index in specific material layers, changes in air gap thickness, and changes in the angle of incidence for light pulses incident on multilayer distributed Bragg reflectors (DBRs). The model determines how these changes affect transmittance, transmittivity phase and optical delay in a given multiplayer structures.

I used a Pentium III[®]-based personal computer with 128 megabytes of random access memory (RAM). This computer used the Windows 98[®] operating system. I used 'Matlab' [1] and 'Mathcad' [2] software packages to develop these models. The Matlab functions were saved as pcode to reduce the run time of the programs. The Matlab pcode is a pre-parsed pseudo-code file of a Matlab m-file which runs faster.

3.2 Index of Refraction

The index models for $\text{Al}_x\text{Ga}_{1-x}\text{As}$ were developed using articles written by Deri [3] and Jenkins [4]. Figure 3-1 displays dispersion data from both models. Jenkins' model was optimized between 0.4 μm and 1.2 μm while Deri's model was optimized to operate between 0.75 μm and 1.5 μm to an accuracy in index of ± 0.002 . However, if this accuracy is reduced to ± 0.02 , the range can be extended to 1.7 μm . Hence, the

two models covered the wavelengths of interest. The models only consider the real part of the

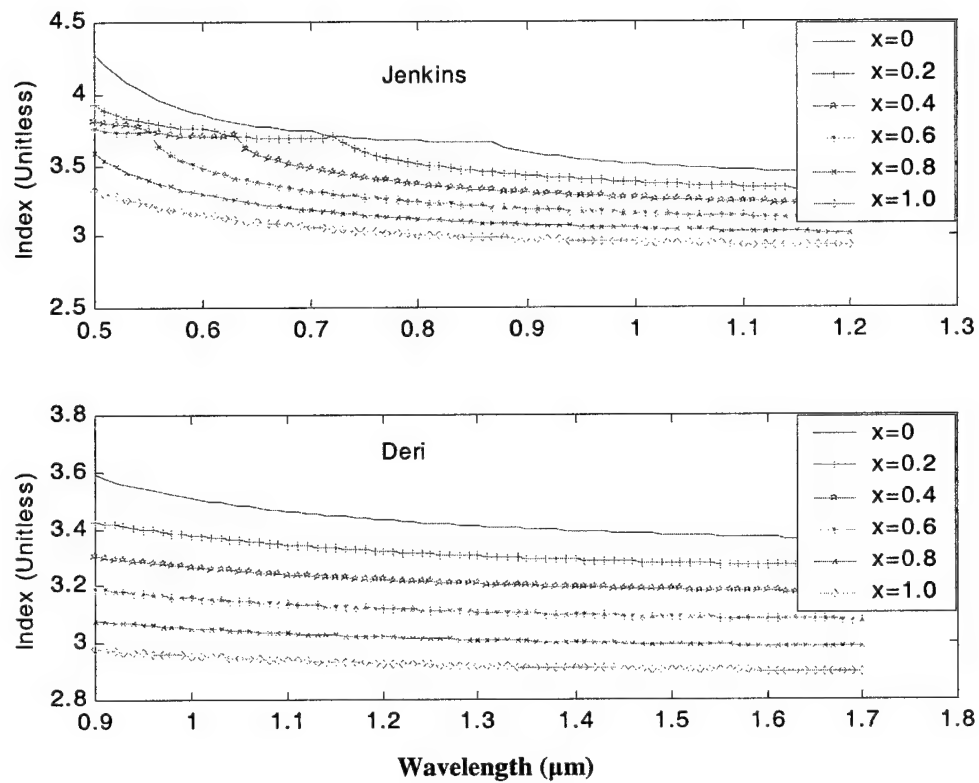


Figure 3-1: Simulation of refractive index data for $\text{Al}_x\text{Ga}_{1-x}\text{As}$ for several values of AlAs mole fraction versus wavelength using the (top) Jenkins' [3] model and the (bottom) Deri's [2] model.

refractive index. Both models were implemented as m-files in Matlab [1]. The program takes the wavelength and composition of AlAs in the $\text{Al}_x\text{Ga}_{1-x}\text{As}$ material as input. The output is the real part of the refractive index that corresponds to the inputs. The models compared well to data presented by Aspnes [5]. Air was assigned a refractive index of 1.

The change of refractive index in the QWs due to the application of an electric field is modeled using Feng's [6] data (See Figure 2-13). Feng's refractive index data is converted to a function in Matlab and used to produce dispersion files corresponding to the various electric field strengths.

3.3 Reflectance and Transmittance Amplitude and Reflectivity and Transmittivity Phase

Power reflectance and transmittance parameters are modeled using the matrix method presented in Section 2-3. Equation 2-11 is used as the core of the model because it allows the angle of incidence and the material thickness to be varied. In this model, the substrate is treated as an infinitely thick layer. The model is implemented in Matlab, and is broken down into several functions to facilitate easy manipulation. The inputs to this program are: angle of incidence, material dispersion data, design wavelength, and the physical structure to be modeled.

Tilting the structure is modeled as a change in the angle of incidence while varying the air-gap within a structure is modeled as a change in the thickness of an air only layer or layers within the structure. To model the change in QW index due to an applied electric field, Feng's data corresponding to a given applied electric field is used. Figure 3-2 displays various modeling results for a 12 period quarter-wave

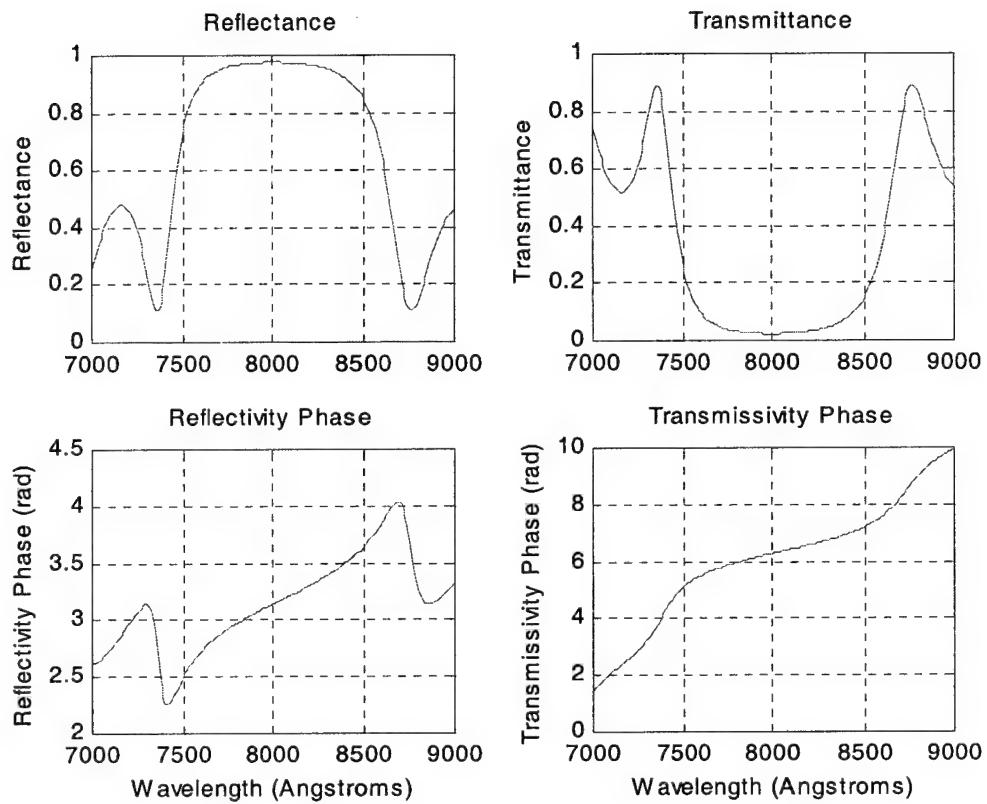


Figure 3-2: Calculated reflectance and transmittance amplitude and reflectivity and transmissivity phase data for a 12-period GaAs/AlAs distributed Bragg reflector on a GaAs substrate. The Bragg design wavelength is 800 nm. Note that $\phi = \pi$ (reflectivity) and $\phi = 2\pi$ (transmittivity).

AlAs/GaAs DBR structure over a wavelength range of 700 nm to 900 nm. The results compare favorably to work done by Nelson and others [7].

3.4 Pulse Delay

The optical input pulse is modeled as a Gaussian function because this function is easy to implement both in the time and frequency domain. The Fourier Transform of a Gaussian pulse is itself a Gaussian pulse. The pulse was modeled using Equation 2.34 which is

$$E_{in}(t) = Ae^{\frac{-(t-t_0)^2}{2\sigma^2}} e^{j\omega_0 t}$$

where ω_0 is the angular frequency, t_0 is the point in time when the pulse originates, and σ is the full width at half maximum (FWHM) of the pulse. The parameter A is the amplitude of the pulse. The pulse was modeled in Matlab and the fast Fourier Transform (FFT) and inverse FFT were used to transform the pulse to and from the frequency domain. $\sqrt{2\ln 2}$ times The inputs to this function include the FWHM of the pulse, the starting time, the number of points to be generated, and the length of time to be considered for the calculations. The function also takes the transmittance $T(\omega)$ and transmittivity phase $\theta(\omega)$ as inputs. For the program to give reliable results, the number of points used must be large enough to reduce aliasing. If the number of points in the pulse and the number of points in the transmission and transmittivity phase is not the same, Matlab will not run the program.

The exiting pulse is modeled as a phase shift in the frequency domain due to changes in the transmittivity phase of the structure and an amplitude change due to changes in the transmittance of the structure such that

$$E_{out}(\omega) = E_{in}(\omega)T(\omega)e^{-i\phi(\omega)} \quad (3-1)$$

where $T(\omega)$ is the transmittance, $\phi(\omega)$ is the transmittivity phase of the structure, and $E_{in}(\omega)$ and $E_{out}(\omega)$ are the input and output pulse in the frequency domain.

The phase shift leads to a time shift when the pulse is transformed to the time domain. Also, a change in transmittance is seen as a change in the amplitude of the pulse in the time domain. Figure 3-3 demonstrates both a phase advancement and a change in amplitude for an example input pulse when both the phase and amplitude of this input pulse is changed in the frequency domain.

3.4 Summary

This chapter describes the models used in this thesis. Reflectance, transmittance and transmittivity phase was modeled in Matlab using the transfer matrix method. The electric field dependence of refractive index in the QW structure was modeled as an interpolation function in Matlab using data presented by Feng [6]. The variable air gap structure was modeled in Matlab by increasing or decreasing the thickness of the air layers in the transfer matrix code. The variable angle of incidence structure was modeled by changing the angle of incidence to the transfer matrix code. The pulse was modeled as a Gaussian function with a central frequency ω_0 . The dispersion data was modeled using published results from Deri [3] and Jenkins [4].

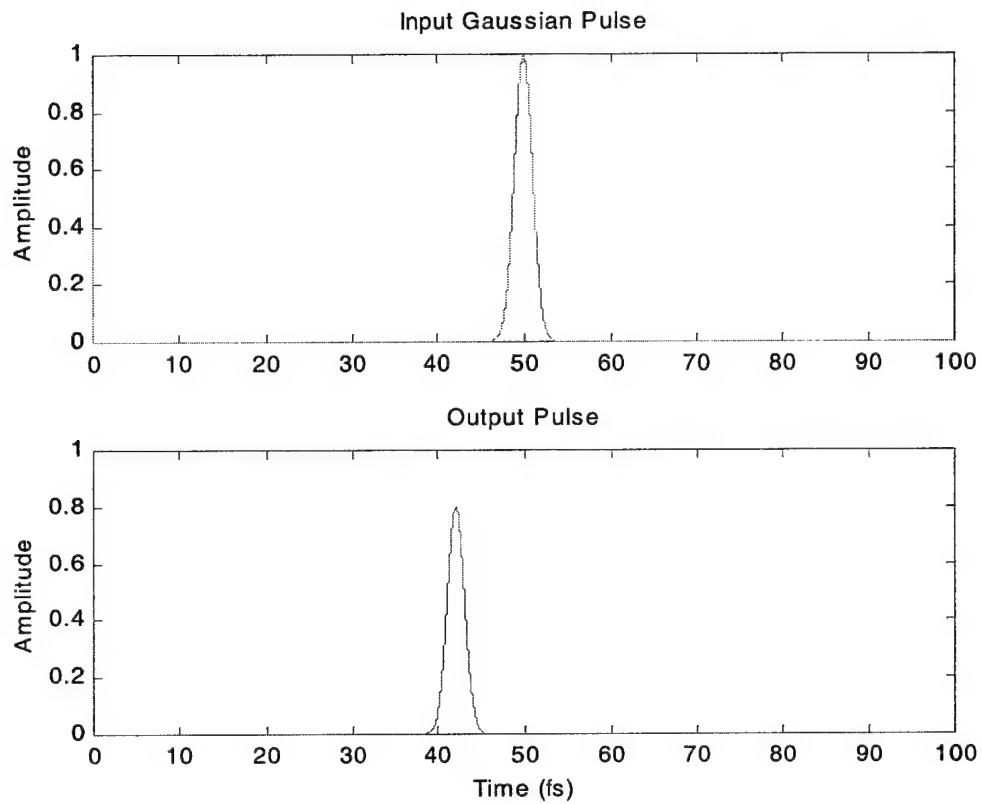


Figure 3-3: Modeled (top) input pulse and (bottom) output pulse after a π linear phase shift and a 0.8 amplitude scaling is added in the frequency domain to a Gaussian pulse. The sampling rate is 10^{-17} s^{-1} and the angular frequency is $1.215 \times 10^{15} \text{ rad/sec}$.

References for Chapter 3

- [1] T. MathWorks, "Matlab Student Version," , 5.3.0 (R11) ed. Natick, MA: The Mathworks Inc., 1999.
- [2] Mathsoft, "Mathcad 2000," , 2000 ed: Mathsoft Inc, 1999.
- [3] R. J. Deri and M. A. Emmanuel, "Consistent Formula for the Refractive Index of $\text{Al}_x\text{Ga}_{1-x}\text{As}$ Below the Band Edge," *Journal of Applied Physics*, vol. 77, pp. 4667-4672, 1995.
- [4] D. W. Jenkins, "Optical Constants of $\text{Al}_x\text{Ga}_{1-x}\text{As}$," *Journal of Applied Physics*, vol. 68, pp. 1848-1853, 1990.
- [5] D. E. Aspnes, S. M. Kelso, R. A. Logan, and R. Bhat, "Optical Properties of $\text{Al}_x\text{Ga}_{1-x}\text{As}$," *Journal of Applied Physics*, vol. 60, pp. 754-767, 1986.
- [6] H. Feng, M. Sugiyama, K. Tada, and Y. Nakano, "Field Induced Optical Effect in a Five-Step Asymmetric Coupled Quantum Well with Modified Potential," *IEEE Journal of Quantum Electronics*, vol. 34, pp. 1197-1208, 1998.
- [7] T. R. Nelson, J. P. Loehr, X. Qianghua, J. E. Ehret, J. E. Van Nostrand, L. Gamble, D. K. Jones, S. T. Cole, R. A. Trimm, W. M. Diffey, R. L. Fork, and A. S. Keys, "Electrically Tunable Group Delays Using Quantum Wells in a Distributed Bragg Reflector," *SPIE*, vol. 3714, pp. 12-23, 1999.

4.0 Device Design

4.1 Introduction

In this chapter I describe my test structure designs. Several methods for the purposeful introduction of a transmittivity phase change and thus an optical pulse delay are given in Chapter 2. The first is a bandpass filter DBR structure with embedded quantum well (QW) absorbing layers in each high index layer. An applied transverse electric field changes the refractive index of the QW layers and hence the delay experienced by light propagating through the structure. The second method relies on varying the size of one or more variable air gaps within a DBR structure to change transmittivity phase and hence the delay experienced by light propagating through the structure. The third method changes the optical delay by varying the angle of incidence of the incoming light.

All the methods mentioned above accumulate phase change through a shift in transmittance passband and transmittivity phase. Equation 2-25 indicates that to get a large phase delay, I must design my structures to have a large transmittivity phase slope at the wavelength of interest. This is the primary basis for my designs. For each method, I will design appropriate multilayer filters with a large transmittivity phase at the operating wavelength. I also design the structures with a wide transmittance passband to allow the transmission of a wide band of frequencies around the operating frequency. The last consideration here is to make the passband of the filters highly transmitting and constant (less than 10% variation with wavelength).

4.2 MQW Device Design

There are several things to consider when designing this structure. Some of the more important ones are wavelength of operation, passband size, variation in transmission, materials used, and placement and number of QWs to be used.

The high index layers are $\text{Al}_{0.3}\text{Ga}_{0.7}\text{As}$ and the low index layers are AlAs. This is pre-determined by Feng's [1] work. I need to operate at a wavelength where absorption is small but the change in refractive index is large. Looking at Feng's [1] data, (Figures 2-12 and 2-13), absorption essentially goes to zero at wavelengths greater than 807 nm. However, the refractive index change is also diminishing after 807 nm. This is not a significant problem because the decrease in refractive index after 807 nm is very small.

The next consideration was the bandwidth necessary for operation. I decided to use a DBR transmittance passband of greater than 40 nm because it is easier to design a flat passband with a wider passband. This corresponds to more than 1.5 THz in bandwidth for wavelengths near 810 nm.

I also needed the transmittance within the passband to change by less than 10% when an electric field up to 50 kV/cm is applied. If the signal power is modulated by greater than 10% when it propagates through the delay element, the output signal will be distorted and possibly useless for the given application.

For the applications this device is designed for, a phase change of 2π or more is necessary. Hence I need to place a sufficient number of QWs within the filter to cause a big change in the phase of the device while maintaining a high transmittance.

The filter design is based on the Fabry Perot Equations 2-18, 2-19, and 2-20. If $R_1 = R_2$ in these equations, then

$$T_0(\lambda) = \frac{(1-R_1) \cdot (1-R_1)}{(1-\sqrt{R_1 R_1})^2} = 1 \quad (4-1)$$

Using a $\lambda/2$ spacer region would make the sin term in Equation 2-18 ≈ 0 . Hence $T(\lambda) = T_0(\lambda) = 1$. If more than one spacer region is incorporated in the design then more dips are seen in the high reflectance band. This can also be correlated to a steeper transmittivity phase at the design wavelength. However, though this is desirable, it also causes bigger ripples in the pass band and increases the size of the structure very rapidly. This has implications for growth and the size of the voltage needed to produce the required electric field across the. When the appropriate interfaces are added, the dips become more pronounced and a high transmittance band develops between those dips. These results are demonstrated in Figure 4-1.

Placing QWs only in the spacer region potentially reduces the voltage necessary to cause delay within the structure. Feng's experiments use up to 50 kV/cm to achieve the changes in refractive index. Hence, the smaller the region over which this field is exerted, the smaller the voltage necessary. If the layers at the top of the first spacer region and bottom of the last spacer region are doped and made into contact regions, the voltage required would be much less than that required to place a field over the whole filter. Placing QWs only in the central spacer region would further reduce the voltage necessary to make a 50 kV/cm field. Designs will be investigated in Chapter 5.

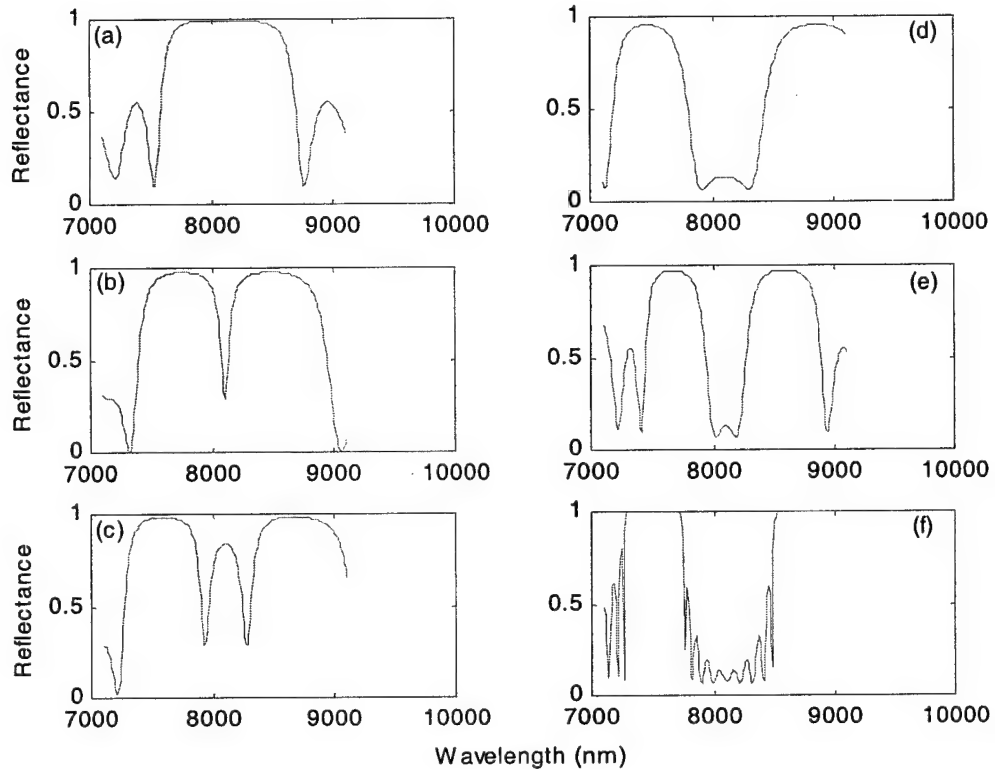


Figure 4-1: Simulated reflectivity spectrum for various Fabry-Perot etalon structures composed of AlAs/GaAs layers. The design wavelength is 810 nm. H and L represent high and low index quarter wave layers.

- (a) $(HL)^8H(LH)^8$ (b) $(HL)^8H^2(LH)^8$ (c) $(HL)^6H(HL)^6H(HL)^6$
 (d) $L(HL)^6H(HL)^5H(HL)^5L^2$ (e) $L(HL)^6H^7(HL)^5H^7(HL)^5L^2$
 (f) $L(HL)^6H(HL)^5H(HL)^5L...H(HL)^5L^2$.

When the reflectances of the reflectors are equal, dips in reflectance is observed. Using multiple reflector and spacer regions results in multiple dips. The use of admittance matched interfaces between the external media and the structure creates an extended region of low reflectivity between dips (passband). Increasing the size of the spacer region reduces the passband.

I explore placing the QWs in different places within the structure. One possibility is placing QWs in all the high layers. Another is to place the QWs in only the spacer regions. A third method is to place the QWs only in the central spacer region. Each design has advantages. By placing QWs in all AlGaAs regions, the number of layers necessary to get a specific amount of delay may be reduced. Hence, the structure will be smaller and faster to grow. However, placing QWs in only the spacer regions reduces the voltage needed to operate the device. Here is the structure I designed to test the effects of changing the refractive index on the transmittance and transmittivity phase

$$L (HL)^5 (H)^5 (HL)^4 (H)^9 (HL)^4 (H)^5 (HL)^4 L \quad (4-2)$$

where L and H represent low and high index $\lambda/4$ layers respectively and the superscript indicates the number of times a layer is repeated. The $(HL)^n$ pairs are reflectors and the H^n layers are spacer regions. This structure can be modified by varying the number or size of the spacer layers, or by varying the number or size (number of periods) of the reflectors. I designed this structure based on the Fabry-Perot etalon and used only three microcavities to limit the amount of ripple in the pass band.

The number of quantum wells that can be placed in each $Al_{0.3}Ga_{0.7}As$ layer was calculated using the following method. First I determined that a 100 Å barrier was sufficient for separating the quantum wells from each other. This is the typical distance used for decoupling wells. The next step was to calculate the optical thickness of the H layer at the operating wavelength, i.e. $(\lambda/4) \sim 637$ Å thick quarter-wave layer at 810 nm. Next I converted all the well components including barriers into optical thickness values using the layer's actual thickness and refractive index at the design wavelength. The optical thickness of Feng's [1] quantum well structure is 65 Å per well and 100 Å per

barrier. The last step is to determine how many wells can fit within the high layer by dividing the optical layer thickness by the optical well thickness as calculated above. I was able to fit 14 QWs in 5 quarter-wave high index layers. Only two QWs can be placed in a single high index quarter-wave layer.

The change in index that Feng [1] calculated was only for the QW region and did not include the barrier regions. Hence the refractive index in the barriers is assumed not to change with the applied electric field. To account for this in my model, I found the proportion of the optical thickness of the well and barrier layers which was due only to the well thickness and used that fraction as a correction factor – about 30% to 40% (depending on the size of the layer). I used this to adjust the change in refractive index.

The transmittivity phase and transmittance of these structures change at the design wavelength when the refractive index of the various layers is increased. Figure 4-2 illustrates the changes in transmittivity phase when the refractive index of various layers is changed by 2% for structures similar to the one presented in Equation 4-1. The simulation included a GaAs substrate and a design wavelength of 810 nm. The slope of the transmittivity phase is the same in all cases because the same number of microcavities is used. Increasing the number of microcavities present can increase the sensitivity of the phase change to a change in refractive index.

4.3 Variable Air-Gap Device

The goal of this design is to produce a DBR structure containing one or more air gaps, whose transmittivity phase can be changed without changing the transmittance of the device significantly at the design wavelength. I used $\text{Al}_{0.1}\text{Ga}_{0.9}\text{As}/\text{AlAs}$ as my high and low index materials.

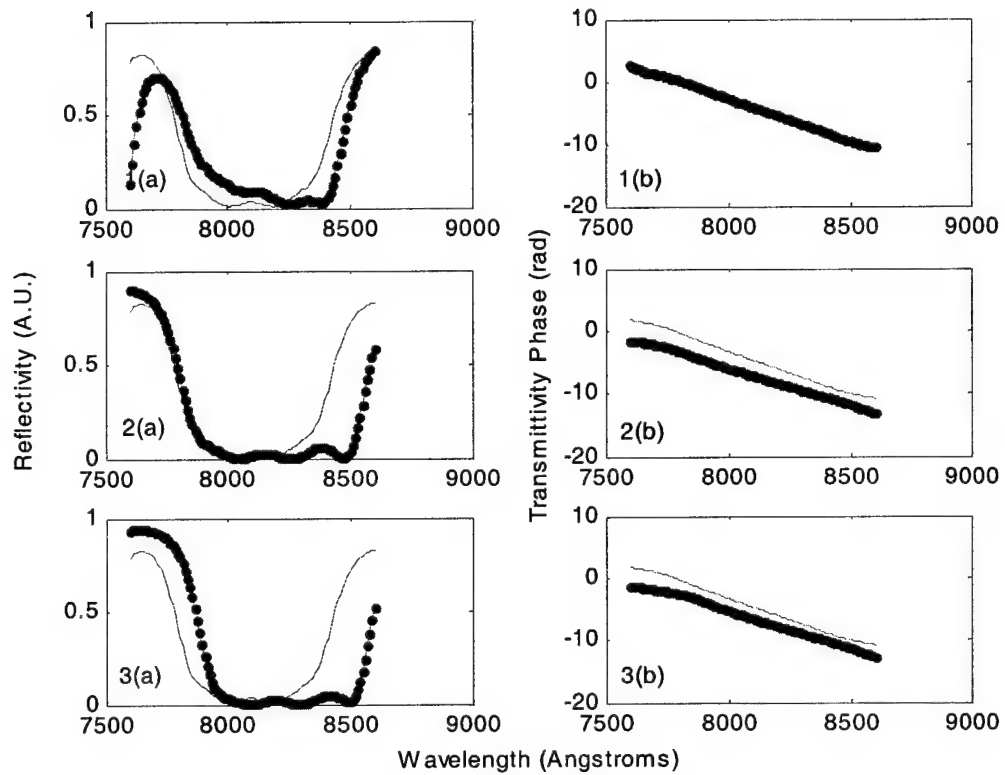


Figure 4-2: The plots on the left are calculated reflectance spectra and those on the right are transmittivity phase spectra for bandpass filters before and after the refractive index of the high index layer is increased by 2%. The thicker lines represent the structures with increased index. All structures contained the same number of modified index layers. 1(a,b) The index of the central spacer region only was increased. 2(a,b) The index of all spacer regions were changed. 3(a,b) The index of all high layers were increased.

$L(HL)^5(H)^5(HL)^4(H_m)^{19}(HL)^4(H)^5(HL)^4L$ is the structure used in (a)

$L(HL)^5(H_m)^5(HL)^4(H_m)^9(HL)^4(H_m)^5(HL)^4L$ is the structure used in (b) and

$L(H_mL)^5(H_m)^3(H_mL)^4(H_m)^9(H_mL)^4(H_m)^3(HL)^4L$ is the structure used in (c)

where H and L are high and low index layers respectively and H_m are the modified index layers.

The material system used is $Al_{0.3}Ga_{0.7}As/AlAs$ on a GaAs substrate. The central wavelength is 810 nm.

To simplify this design I decided to use only $\lambda/4$ layers and to consider only light impinging the structure at normal incidence. The design is accomplished by using a computational algorithm in Mathcad, which searches for elements of the 2x2 matrix that give significant phase change and high transmittance. Designs for two and four air gaps were investigated.

I used Equation 2-10 as the basis of the computational algorithm. If the angle of incidence is 0° and the layers are $\lambda/4$ -thick, the matrix in Equation 2-10 becomes

$$\begin{bmatrix} 0 & \frac{i}{n_m} \\ in_m & 0 \end{bmatrix} \quad (4-2)$$

where n_m is the refractive index of the m^{th} layer. If several layers are cascaded together the 2x2 matrix representation becomes

$$\begin{bmatrix} 0 & \pm ix \\ \pm \frac{i}{x} & 0 \end{bmatrix} \quad (4-3)$$

for a stack containing an odd number of layers and

$$\begin{bmatrix} \pm y & 0 \\ 0 & \pm \frac{1}{y} \end{bmatrix} \quad (4-4)$$

for a stack containing an even number of layers, where x and y are index product terms

such that $x = \prod \frac{n_{i+1}}{n_i n_{i+2}}$ and $y = \prod \frac{n_{i+1}}{n_i}$ for $i = 1, 2, 3, \dots$, where n_i represents the

refractive index of each $\lambda/4$ layer present in the structure.

By utilizing Equations 2-10 and 2-13 and the simplified odd stack representation in Equation 4-2, I modeled a double air gap structure using

$$\begin{bmatrix} 0 & ia \\ \frac{i}{a} & 0 \end{bmatrix} \begin{bmatrix} \cos(2\pi d) & i \sin(2\pi d) \\ i \sin(2\pi d) & \cos(2\pi d) \end{bmatrix} \begin{bmatrix} 0 & ib \\ \frac{i}{b} & 0 \end{bmatrix} \begin{bmatrix} \cos(2\pi(0.5-d)) & i \sin(2\pi(0.5-d)) \\ i \sin(2\pi(0.5-d)) & \cos(2\pi(0.5-d)) \end{bmatrix} \begin{bmatrix} 0 & ic \\ \frac{i}{c} & 0 \end{bmatrix} \begin{bmatrix} 1 \\ n_s \end{bmatrix} \quad (4-5)$$

where the only unknowns are a , b and c , and the optical thickness of the air gap d . The value of n_s is the refractive index of the substrate at $1.55 \mu\text{m}$, the design wavelength. I then calculated transmittivity phase and transmittance for every combination of a , b and c between 0.1 and 2 for values of d from 0λ to 0.5λ . I then sorted out the values of a , b and c which gave less than a 10% change in transmittance, for which transmittance is greater than 0.7, and for which transmittivity phase changed by more than 0.5 radians. Figures 4-3 and 4-4 depict plots for the successful values of a , b and c which meet the limiting criteria. From these values of a , b and c , I then used Figure 4-5 to determined the practical structure whose matrix element came closest to a , b and c . Figure 4-5 is a representation of possible values of element (1,2) in a 2×2 matrix for an $\text{Al}_{0.1}\text{Ga}_{0.9}\text{As}/\text{AlAs}$ DBR structure with an odd number of layers. I can only use odd layers because the DBR used in the simulation is limited to only odd layered structures. Figure 4-6 depicts the spectrum of a practical structure derived from Figure 4-5. The calculated structure is $(\text{LH})^{11}\text{L}(\text{air})^2(\text{LH})^{11}\text{L}(\text{air})^2(\text{LH})\text{L}$ where H and L are the high and low index quarter-wave layers respectively and air is the variable air gap layers. The superscript indicates the number of repetitions used. Figure 4-7 depicts the transmittance and transmittivity phase verses air gap thickness at $1.55 \mu\text{m}$ for that structure.

This structure can be actuated by using electrostatic forces to move the DBR cantilever between the air gap. The method for doing this is presented in Section 1.2.2.

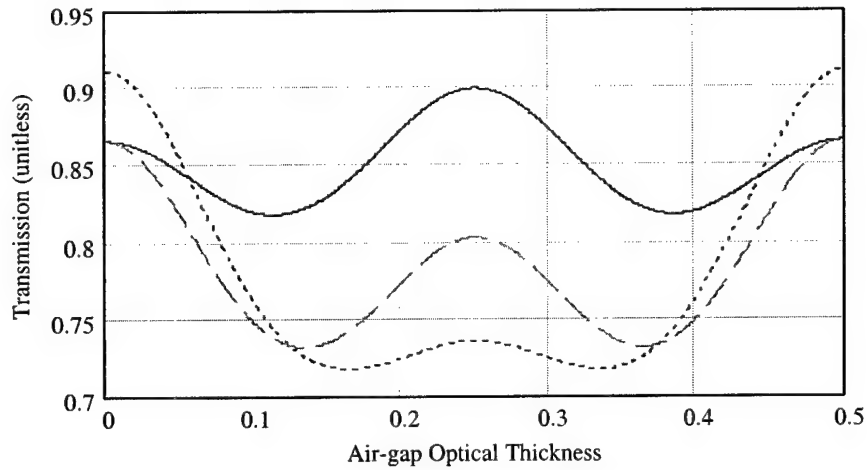


Figure 4-3: Simulation of transmittance verses air gap size for the values of a , b and c calculated using my computational algorithm. For the solid line the values of a , b and c are 0.7, 0.7 and 0.8 respectively. For the dotted line the values of a , b and c are 1.55, 1.55 and 0.4 respectively. For the dashed line the values of a , b and c are 0.65, 0.65 and 0.8 respectively.

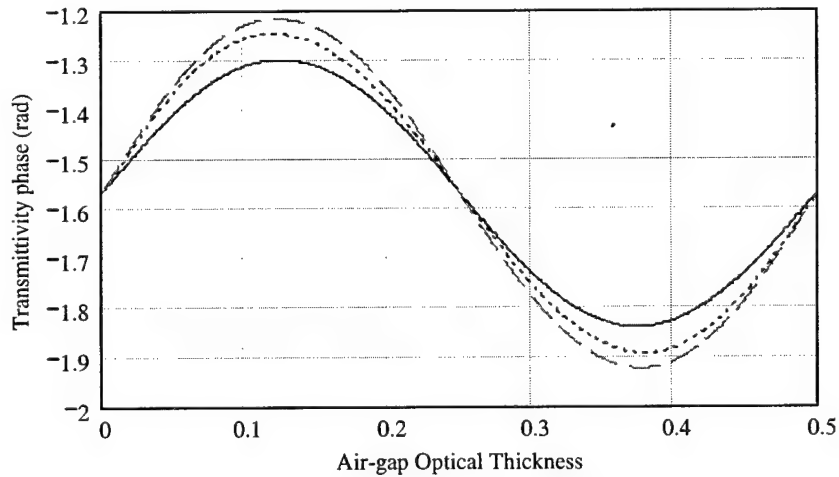


Figure 4-4: Simulation of transmittivity phase verses air gap size for the values of a and c calculated using my computational algorithm. For the solid line the values of a , b and c are 0.7, 0.7 and 0.8 respectively. For the dotted line the values of a , b and c are 1.55, 1.55 and 0.4 respectively. For the dashed line the values of a , b and c are 0.65, 0.65 and 0.8 respectively.

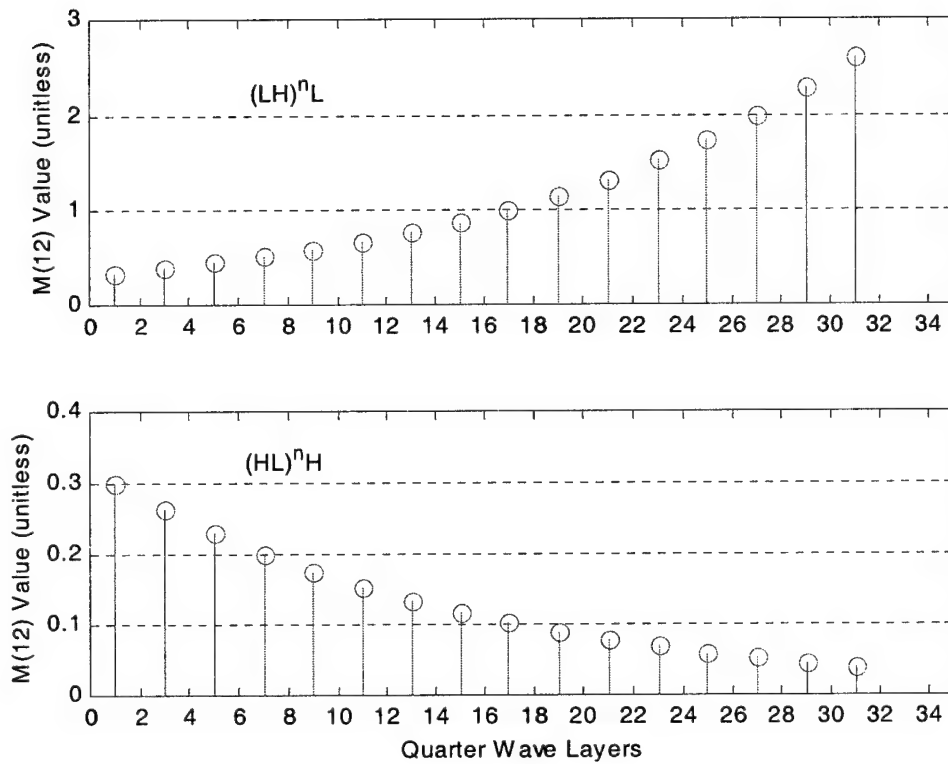


Figure 4-5: Simulation of values of x in Equation 4-3 for various odd numbers of layer combinations. The calculations were done at $1.55 \mu\text{m}$. The top graph depicts $(LH)^n L$ layered structures while the bottom graph depicts $(HL)^n H$ layered structures. L and H indicate low and high index layers respectively. The superscript n represents the number of times the pair in brackets is repeated.

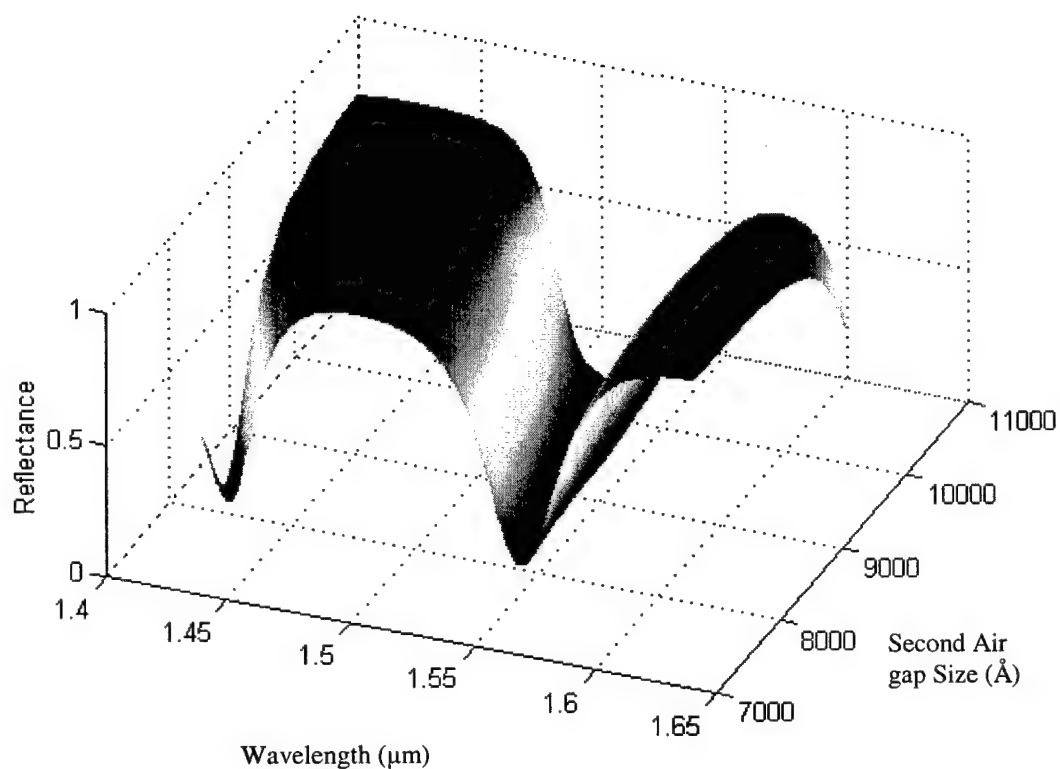


Figure 4-6: Simulation of reflectance versus wavelength as the air gap sizes are varied for the $(\text{LH})^{11}\text{L}(\text{air})^2(\text{LH})^{11}\text{L}(\text{air})^2(\text{LH})\text{L}$ DBR. The material used is $\text{Al}_{0.1}\text{Ga}_{0.9}\text{As}/\text{AlAs}$. Both air gaps are 0.5λ – thick (7750 Å) in the rest position. The central wavelength is 1.55 μm. The thickness of the second air gap is represented on the graph. When the thickness of one air gap is increased, the thickness of the other is reduced by the same amount.

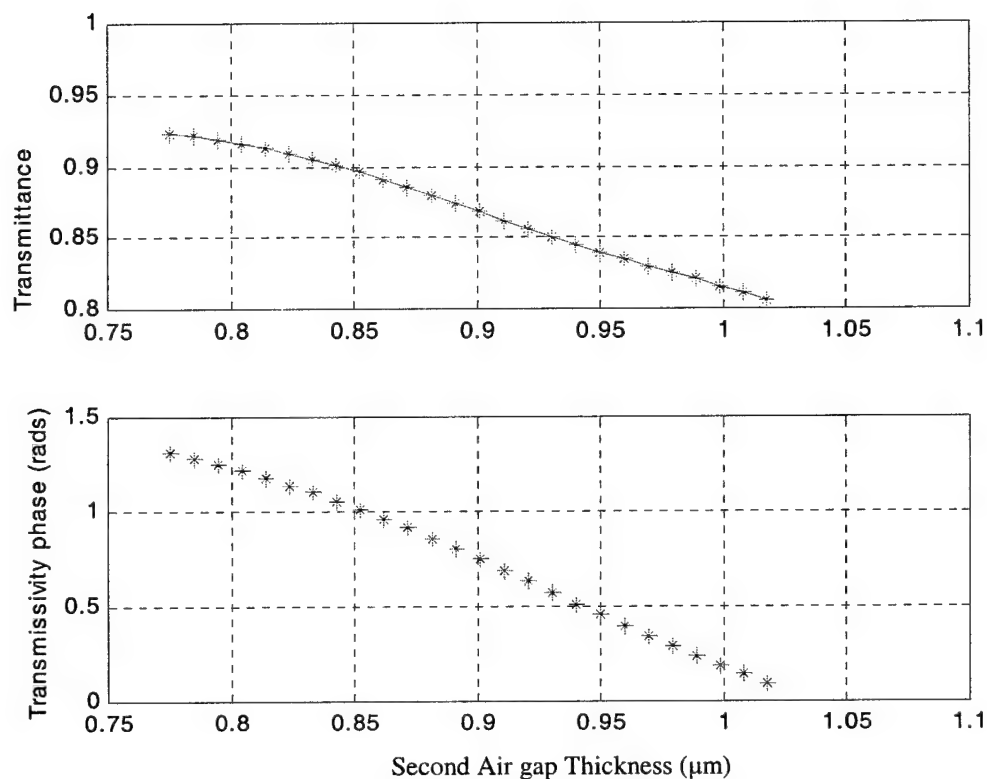


Figure 4-7: Simulation of the transmittance (top) and transmissivity phase (bottom) versus air gap thickness at a wavelength of $1.55\mu\text{m}$ for the $(\text{LH})^{11}\text{L}(\text{air})^2(\text{LH})^{11}\text{L}(\text{air})^2(\text{LH})\text{L}$ DBR. The material is $\text{Al}_{0.1}\text{Ga}_{0.9}\text{As}/\text{AlAs}$. Both air gaps are 0.5λ - thick in the rest position. The thickness of the second air gap is represented as the x-axis on the graph.

4.4 Variable Angle of Incidence Device

This method of optical phase delay consists of changing the angle of incidence of incoming light onto a DBR structure. This has the effect of changing the effective layer thickness. Varying the effective layer thickness causes the reflectivity spectrum to blue-shift. The spectrum of the structure depends on the polarization of the incident light. Therefore both p- and s- polarization must be considered.

The DBR materials used are $\text{Al}_{0.1}\text{Ga}_{0.9}\text{As}/\text{AlAs}$. The design wavelength is $1.55\ \mu\text{m}$ because of the low power loss experienced by this wavelength in commercial glass fiber optic cables. The design can be extended to any wavelength provided that absorption is small in the region of interest.

The structure is essentially a bandpass filter designed using the Fabry Perot equations. The passband was designed to be about 40 nm and extended from $1.53\ \mu\text{m}$ to $1.58\ \mu\text{m}$. The passband is designed so that the reflectance varied by less than 10% when the structure is tilted through at least 50° .

My design used a multilayer Fabry-Perot etalon structure with multiple micro-cavities to create a bandpass filter. The reflectance of each reflector within the structure is less than 5% at the wavelengths of interest. Considering the Fabry-Perot Equations (2-18 to 2-20), when the R_1 and R_2 terms are very small, the phase term is diminished and the transmittance of the structure in the passband remains very high regardless of the size of the cavity. Figure 4-8 is a simulation of my proposed structure as it is tilted through an angle of 40° . Figure 4-9 is the transmittance spectrum and transmittivity phase verses angle of incidence of the proposed structure at $1.55\ \mu\text{m}$.

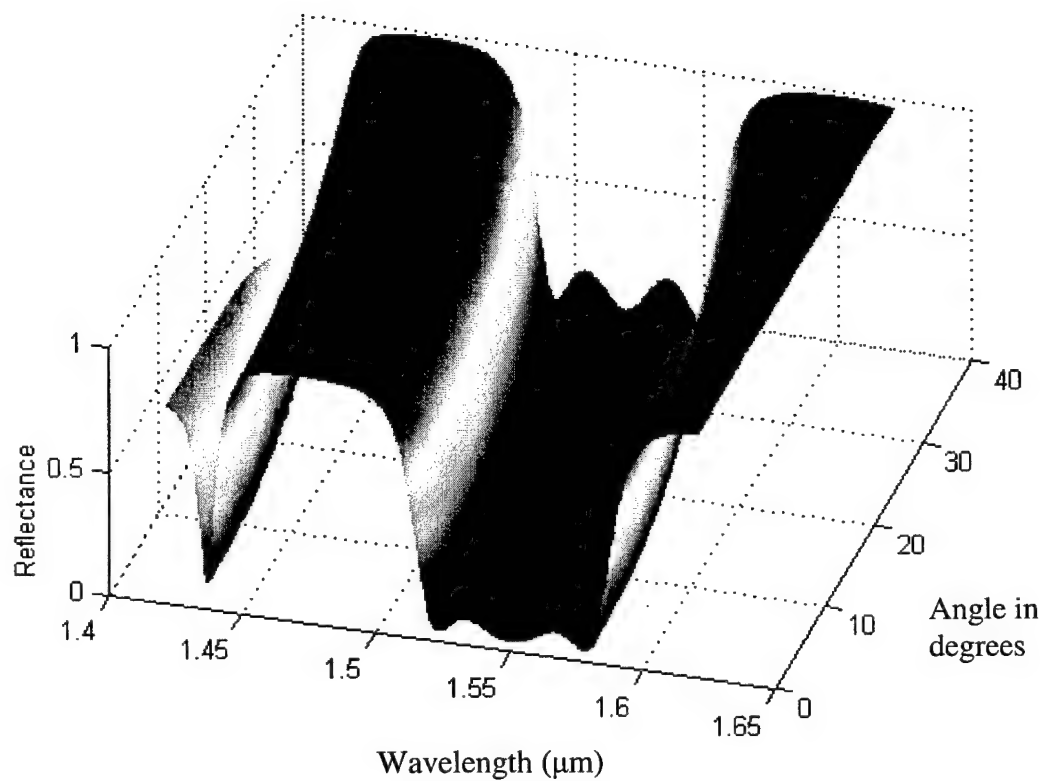


Figure 4-8: Reflectance spectrum of a multilayer bandpass filter versus angle of incidence. The structure of the filter is $L(HL)^5(H)^3(HL)^4(H)^5(HL)^4(H)^3(HL)^4L$ where L and H are high and low index layers respectively and the superscript indicates the number of repeated quarter-wave layers. The materials used are $Al_{0.1}Ga_{0.9}As/AlAs$ on a GaAs substrate.

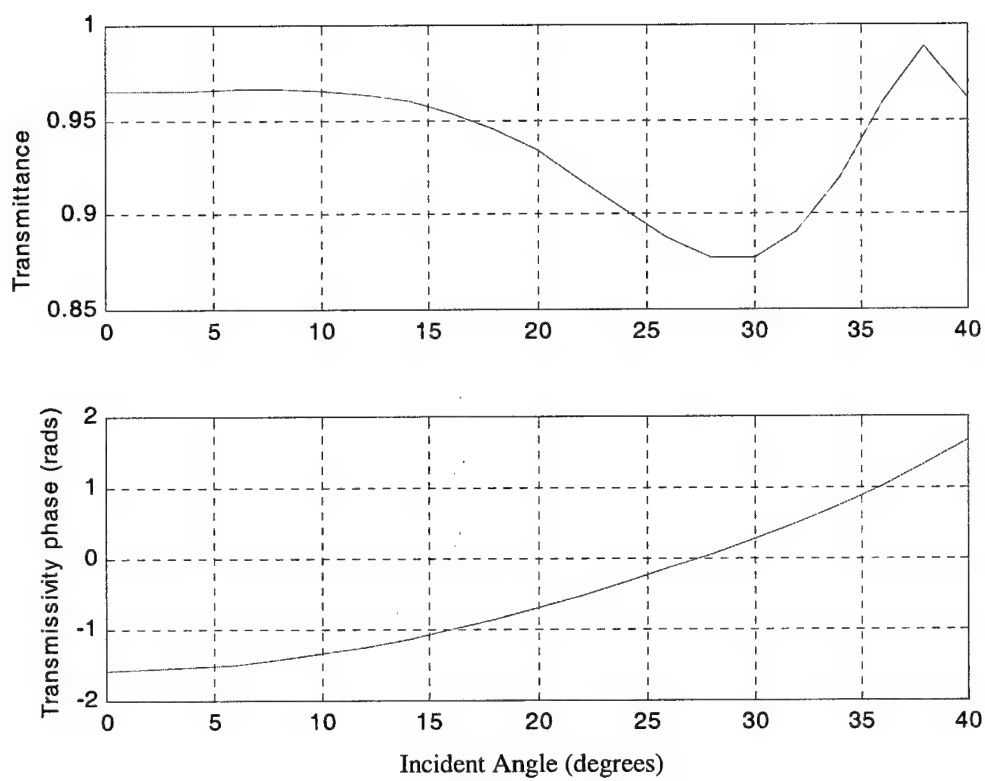


Figure 4-9: Calculated transmittance and transmissivity phase verses angle of incidence for the structure in Figure 4-8 at 1.55 μm .

4.5 Summary

This chapter described the different structures proposed for implementing optical delay using the three methods outlined in Chapter 2. For the MQW method, the design proposed is a 3-cavity bandpass filter. The QWs can be placed in the cavities and/or all the high layers. The structure designed for the variable air gap method is determined using a computational algorithm. One possible design is presented in section 4-3. The design for the variable angle of incidence structure consists of a 3-cavity bandpass filter that can be modified for better results.

References for Chapter 4

- [1] H. Feng, M. Sugiyama, K. Tada, and Y. Nakano, "Field Induced Optical Effect in a Five-Step Asymmetric Coupled Quantum Well with Modified Potential," *IEEE Journal of Quantum Electronics*, vol. 34, pp. 1197-1208, 1998.
- [2] Mathsoft, "Mathcad 2000," 2000 ed: Mathsoft Inc, 1999.

5.0 Results and Analysis

5.1 Introduction

In this chapter I present my numerical studies of the optical delay and dispersion experienced by a Gaussian pulse as it propagates through the test structures I designed in Chapter 4. I assume the amplitude of the input pulse is 1 and the pulse has standard deviation of 0.5 fs. The pulse is centered at 1.55 μm .

In this chapter I also discuss the relative size of the delay experienced by each test structure and qualitatively describe the changes in appearance of the pulse after propagating through the structure. I determine how the delay produced by the structures can be increased and discuss the tradeoffs that arise. One such example is the effect of having greater optical delay on insertion loss and pulse dispersion. Another example is the relationship between optical delay time and device size and fabrication difficulty.

To understand how a pulse which propagates through the structures can be distorted I present a description of the factors which affect the degree of dispersion in the pulse. Finally, I discuss how the design affects the actuation of the device and special considerations that must be explored in each case.

5.2 Dispersion in Dispersive Media

When a pulse propagates through any dispersive media it experiences some distortion. For a Gaussian pulse, if the slope of the transmittivity phase is non-linear, the pulse may contract or expand in the time domain. This is shown in Figure 5-1.

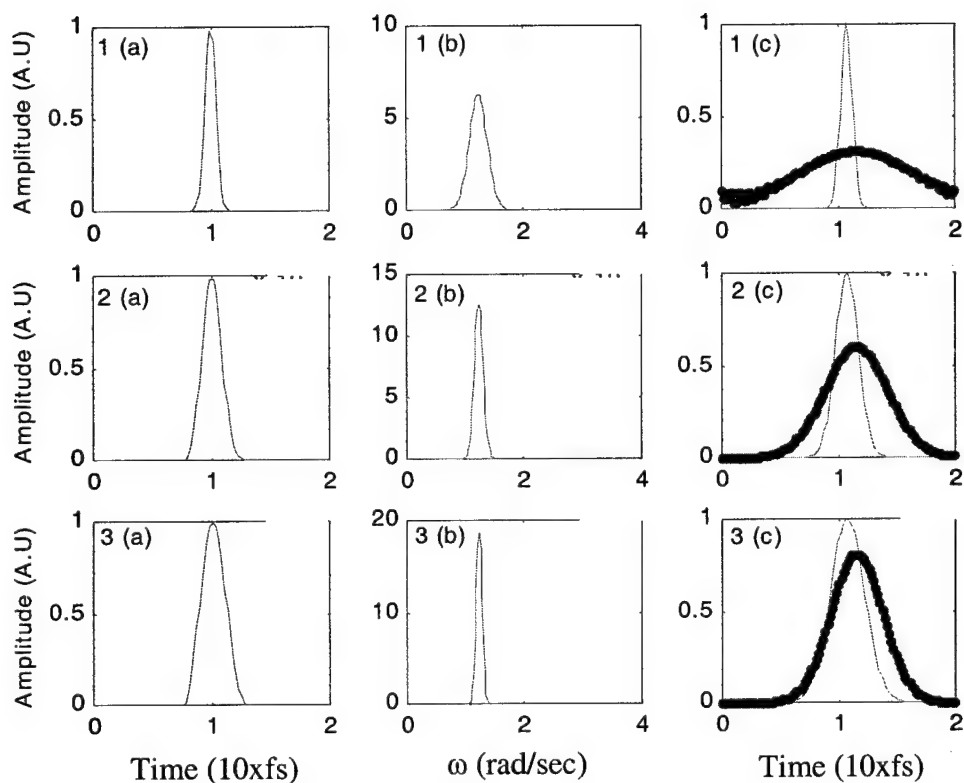


Figure 5-1: Plots 1-3(a) are input pulses with increasing FWHM 1-3(b) are the representation of those pulses in the frequency domain. 1-3(c) depicts the output pulses (dotted) compared to the original input pulse (solid) when the pulses propagate through a dispersive medium (with non linear phase). $\omega_0=1.2153 \times 10^{15}$ rad/sec.

If the slope is linear then no dispersion occurs. However, only the slope of the transmittivity phase near ω_0 is important for sufficiently band limited pulses.

5.3 Multiple Quantum Well Design

A variation of the structure developed in Chapter 4 was used here. The structure is $L(HL)^5H^5(HL)^4H^9(HL)^4H^5(HL)^4L$. Before any field is applied to the structure the passband is flat – i.e. transmittance varies by less than 10%. The width of the passband is about 500 Å. See the solid line graph in Figure 5-2-1(a).

Initially I tested the effect of placing the quantum wells (QW) in various places in the structure when an electric field is placed across it. I tried three different designs; first, I placed the QWs only in the central spacer region; second, I placed the QWs in all the spacer regions; and third, I placed the QWs in all the high index layers present in the structure. Figure 5-2 shows the relationship between the change in the spectrum and QW placement under a 50 kV/cm field.

In all cases the transmittance of the structure remains above 90% in the wavelength region near 810 nm. The transmittivity phase change however, is much smaller for the structure containing QWs only in the central spacer region. This result is expected because that structure contains QWs in only 9 layers compared to 19 layers and 27 layers respectively in the other two structures.

The structure containing QWs in only the central spacer regions is the best choice because it produces fewer ripples in the transmittance passband and the transmittivity phase is smoother. The phase shift for that structure at 810 nm is 6.36 radians. The structure with QWs in all high index layers produces the largest phase shift of 6.48 radians.

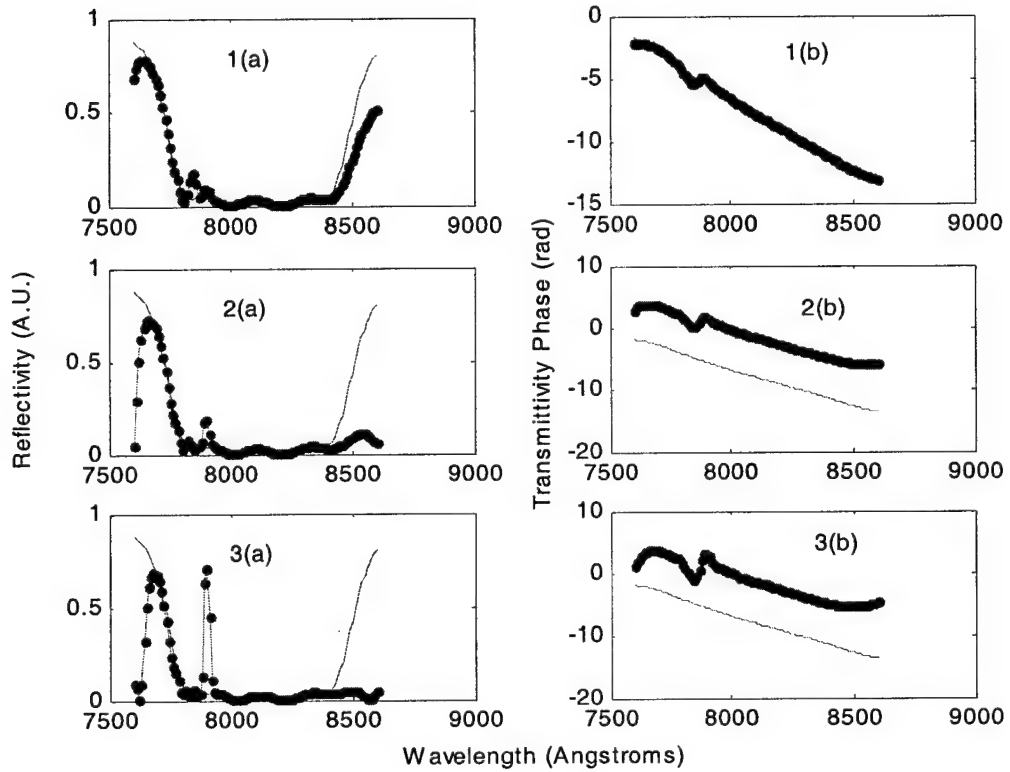


Figure 5-2: Calculated reflectance spectra of a filter with the structure $L(HL)^5H^5(HL)^4H^9(HL)^4H^5(HL)^4L$ quarter-wave layers where L and H represent the low and high index layers respectively. The material system is $Al_{0.1}Ga_{0.9}As/AlAs$ on a GaAs substrate. The solid line graphs are the spectra under no electric field while the dotted line graphs are the spectra when the structure is under a 50 kV/cm electric field. 1(a) and 1(b) are for a structure with QWs only in the central spacer region. The phase shift was negligible. 2(a) and 2(b) are for a structure with QWs in all the spacer regions. The phase shift at 810nm is 6.36 radians. 3(a) and 3(b) are for a structure with QWs in all the high index layers. The phase shift at 810 nm is 6.48 radians.

Next, I decreased the thickness of the center spacer region to determine the effect of this change on the transmittance and transmittivity phase under a 50 kV/cm electric field. Figure 5-2 depicts the relationship for a $L(HL)^5H^5(HL)^4H(HL)^4H^5(HL)^4L$ structure where again 1(a) and 2(a) have QWs only in the spacer region, 1(b) and 2(b) have QWs in all spacer regions and 1(c) and 2(c) have QWs in all high index layers. A decreased central region thickness causes the change in phase with applied electric field to drop by about 1 radian. This drop is expected because less QWs are being used in this design. A thinner central region also expands the passband as described in Chapter 4. However, the passband remains flat near the operating wavelength of 810 nm, varying by less than 10% in all cases. The best results appear again to be the structure with QWs in only the spacer regions because of the smoother phase and flatter transmittance in the passband. It also contains less QWs which make it faster to fabricate.

Next I tested the structure $(L(HL)^5H^5(HL)^4H(HL)^4H^5(HL)^4L$ with QWs only in the microcavities) under varying electric fields, i.e. 10 kV/cm and 50 kV/cm. The results are presented in Figure 5-4. Under both electric fields the transmittance is high (0.95) near the operating wavelength and varies less than 10%.

The change in phase under 10 kV/cm is less than 1 radian while for the 50 kV/cm it is approximately 2π . Figure 5-4-1(c) and 5-4-2(c) display the pulse after it propagates through the structure before and after the respective electric fields are applied. In both cases, both of the pulses show no dispersion and retain their Gaussian shape. This is expected because the transmittivity phase is linear near the operating wavelength.

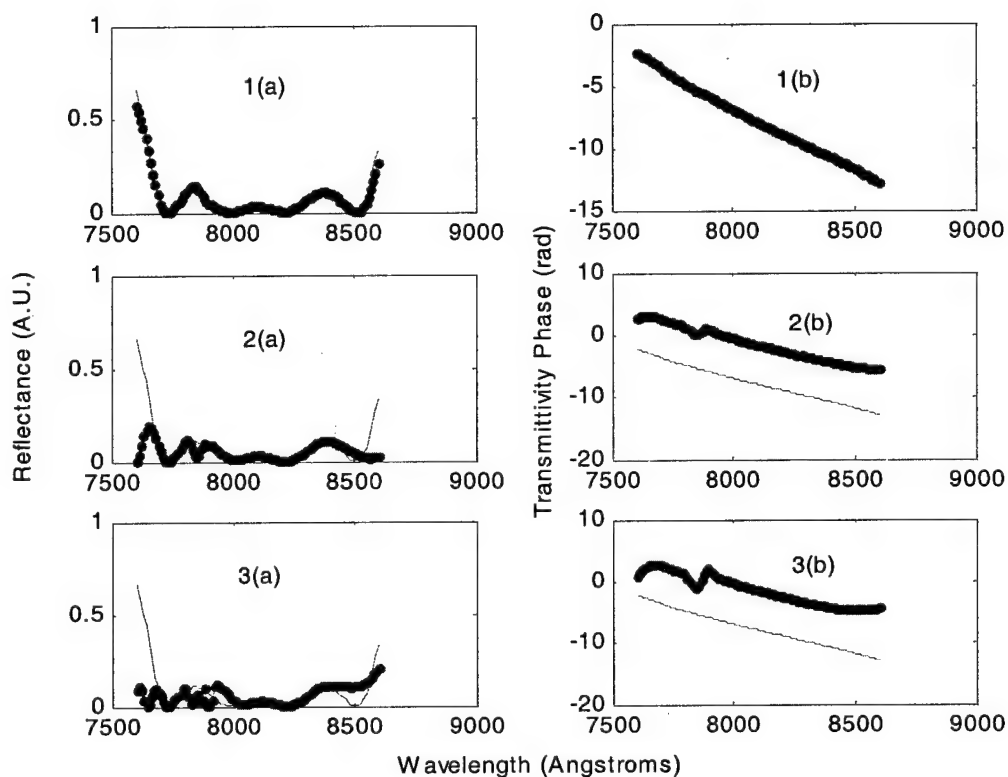


Figure 5-3: Calculated reflectance spectra of a filter with the structure $L(HL)^5H^5(HL)^4H(HL)^4H^5(HL)^4L$ quarter-wave layers where L and H represent the low and high index layers respectively. The material system is $Al_{0.1}Ga_{0.9}As/AlAs$ on a GaAs substrate. The solid line graphs are the spectra under no electric field while the dotted line graphs are the spectra when the structure is under a 50 kV/cm electric field. 1(a) and 1(b) are for a structure with QWs only in the central spacer region. The phase change at 810 nm is negligible. 2(a) and 2(b) are for a structure with QW in all the spacer regions. The phase change at 810 nm is 6.36 radians. 3(a) and 3(b) are for a structure with QWs in all the high index layers. The phase change at 810 nm is 6.48 radians.

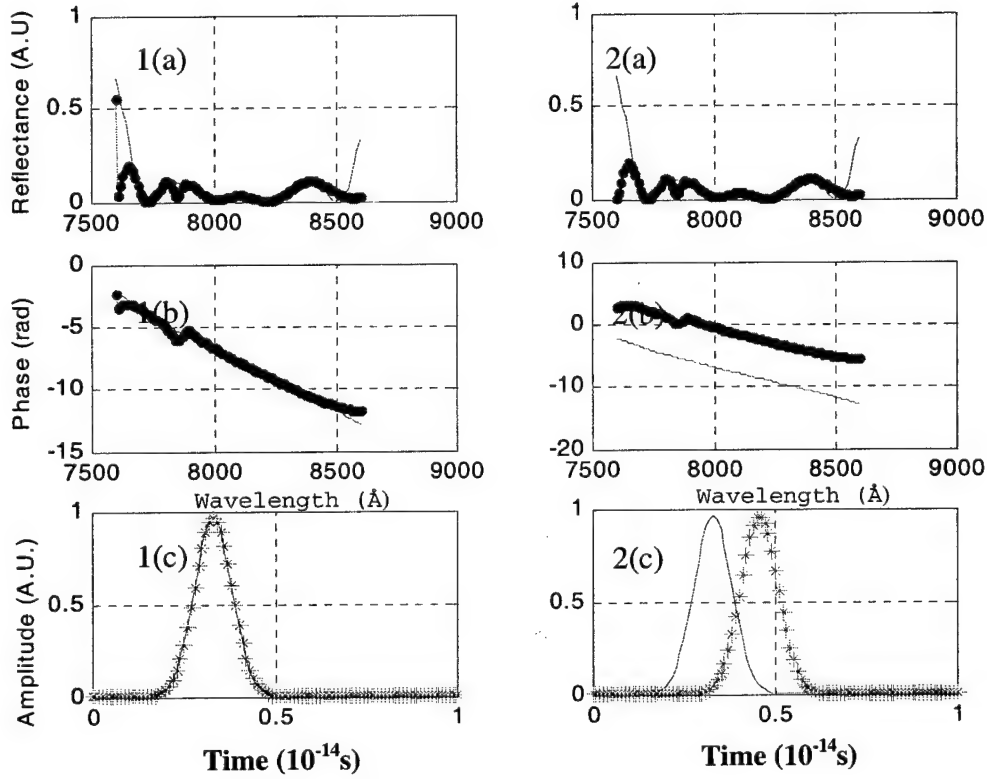


Figure 5-4: Calculated reflectance spectra and pulse delay of a filter with the structure $L(HL)^5H^5(HL)^4H(HL)^4H^5(HL)^4L$ quarter-wave layers where L and H represent the low and high index layers respectively. The material system used is $Al_{0.1}Ga_{0.9}As/AlAs$ on a GaAs substrate. QWs are placed in only the spacer regions. 1(a), 1(b) and 1(c) are for a structure under a 10 kV/cm field. 2(a), 2(b) and 2(c) are for a structure under a 50 kV/cm field. The (a) plots represent reflectivity spectrum, the (b) plots represent transmittivity phase and the (c) plots represent a pulse after propagating through the structure. Solid line plots are for the structure under no field while dotted lined plots are for the structure under the 10 kV/cm or 50 kV/cm field.

The MQW structure produces optical delay when an electric field is applied. The delay time corresponds to the number QW within the structure and to a lesser extent, the location of those wells. Locating those wells only in the central spacer regions greatly reduces the voltage required to operate this device, but may require additional fabrication steps. A quasi-monochromatic pulse experiences very little dispersion when it propagates through this structure.

5.4 Variable Air Gap Structure

I used my algorithm developed in Chapter 4 to find the structures that gave the greatest change in transmittivity phase while maintaining transmittance about 0.7 for both the single air gap and double air gap structures. No solution was found for the single air gap structure (for quarter-wave layers). Several results were found for the double air gap structure. Some are presented in Table 5-1. The M_{12} element of the 2x2 matrix of the equivalent DBR for each segment is recorded as well as an equivalent ($\lambda/4$) structure. The algorithm was optimized for 1.55 μm .

Figure 5-5 and Figure 5-6 display the transmittance and transmittivity phase of three of those structures using the theoretical M_{12} matrix elements. The maximum phase change observed while the limiting conditions are met is 0.8 radians. The cantilever has to move a distance of 0.23λ or 357 nm to get the maximum change.

If the transmittance is allowed to be as low as 50%, greater change in transmittivity phase is achieved. The last row in Table 5-1 shows the M_{12} element of the 2x2 matrix and equivalent $\lambda/4$ structure with these characteristics.

The transmittance and transmittivity phase is demonstrated in Figure 5-7 and 5-8. The transmittivity phase change observed is 1.2 radians, which is an increase of 50% over

Table 5-1

M_{12} Matrix Elements for Double Air Gap Structure for Transmittance > 70%			
Top DBR	Cantilever	Bottom DBR	Equivalent $\lambda/4$ Structure
0.65	0.90	1.50	$(LH)^5L(air)^2(LH)^{11}L(air)^2(LH)^7L$
0.70	0.90	1.50	$(LH)^6L(air)^2(LH)^{11}L(air)^2(LH)^7L$
1.70	0.35	1.50	$(LH)^{12}L(air)^2(LH)^{11}L(air)^2L$
1.95	0.35	1.45	$(LH)^{13}L(air)^2(LH)^{10}L(air)^2L$
2.20	0.30	1.30	$(LH)^{14}L(air)^2(LH)^{10}L(air)^2L$
M_{12} Matrix Elements for Double Air Gap Structure for Transmittance > 50%			
2.36	2.32	1.52	$(LH)^{14}L(air)^2(LH)^{11}L(air)^2L$

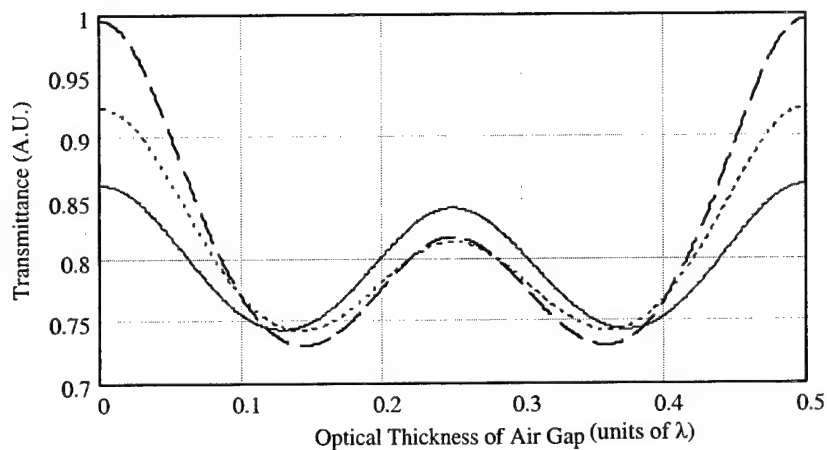


Figure 5-5: Transmittance versus air gap size of a filter using the 2x2 matrix elements described in the first three rows of Table 5-1. The material system used is $\text{Al}_{0.1}\text{Ga}_{0.9}\text{As}/\text{AlAs}$ on a GaAs substrate. The central Bragg wavelength is $1.55\ \mu\text{m}$.

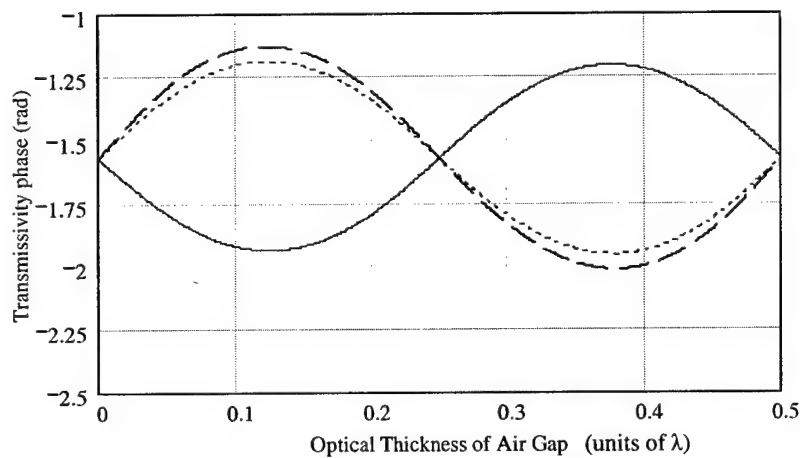


Figure 5-6: Transmissivity phase versus air gap size of a filter using the 2x2 matrix elements described in the first three rows of Table 5-1. The material system used is $\text{Al}_{0.1}\text{Ga}_{0.9}\text{As}/\text{AlAs}$ on a GaAs substrate. The central Bragg wavelength is $1.55\ \mu\text{m}$.

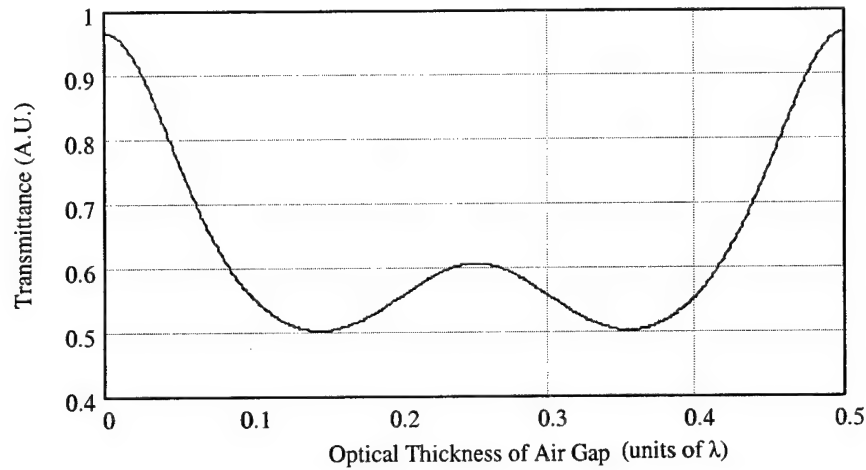


Figure 5-7: Transmittance versus air gap size of a filter using the 2x2 matrix elements described in the last row of Table 5-1. The material system used is $\text{Al}_{0.1}\text{Ga}_{0.9}\text{As}/\text{AlAs}$ on a GaAs substrate. The central wavelength is $1.55\ \mu\text{m}$.

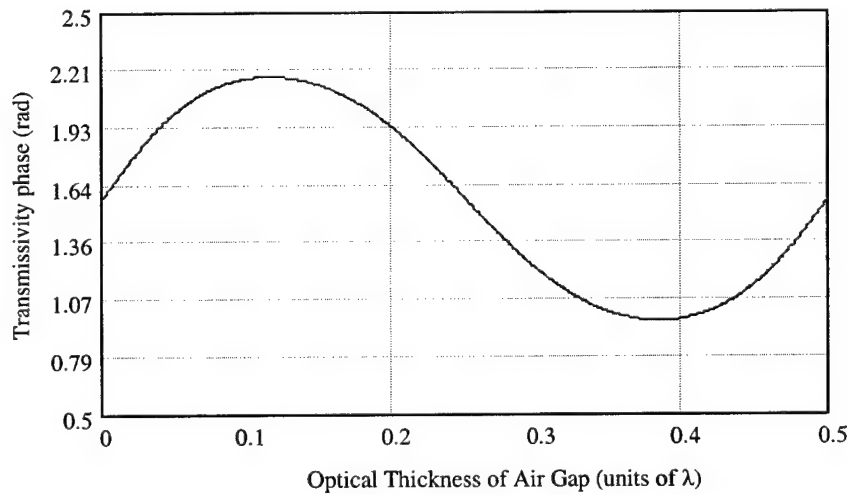


Figure 5-8: Transmissivity phase versus air gap size of a filter using the 2x2 matrix elements described in the last row of Table 5-1. The material system used is $\text{Al}_{0.1}\text{Ga}_{0.9}\text{As}/\text{AlAs}$ on a GaAs substrate. The central wavelength is $1.55\ \mu\text{m}$.

the previous structures. The cantilever has to move 0.25λ or 388 nm for this range of phase change.

Two equivalent ($\lambda/4$) structures are simulated in Matlab to determine the delay a practical structure would produce. Figure 5-9 and 5-10 displays the calculated results for the third and sixth equivalent structure in Table 5-1. Because the equivalent structures are not identical to the structures produced using the search algorithm, the transmittance and transmittivity phase graphs are different. I will give a brief analysis of Figure 5-9 and a more detailed analysis of Figure 5-10.

In Figure 5-9(c) some dispersion is seen by the change in the FWHM of the pulses. A look at Figure 5-9(d) shows that the transmittivity phase spectrum is non-linear near $1.55\ \mu\text{m}$, which causes dispersion. The maximum optical delay experienced by the pulse at the design wavelength is 6.2fs.

The transmittance in Figure 5-10 is higher and varies less than the theoretical model (Figure 5-7). The maximum phase change experienced by this structure is less than the theoretical model - only 1.12 radians ($\sim 9.2\text{fs}$). The cantilever has to move $\sim 390\ \text{nm}$ to produce the full range of phase change. Figure 5-10(c) depicts three pulses after propagating through the structure with the cantilever in different positions. The cantilever range used is between $0.95\ \mu\text{m}$ and $1.4\ \mu\text{m}$. Some pulse dispersion is observed (Figure 5-10(c)) by the change in the FWHM of the pulses. The transmittivity phase spectrum for the structure seen in Figure 5-10(d) is non linear near the central frequency of $1.55\ \mu\text{m}$ which is an indication of dispersion.

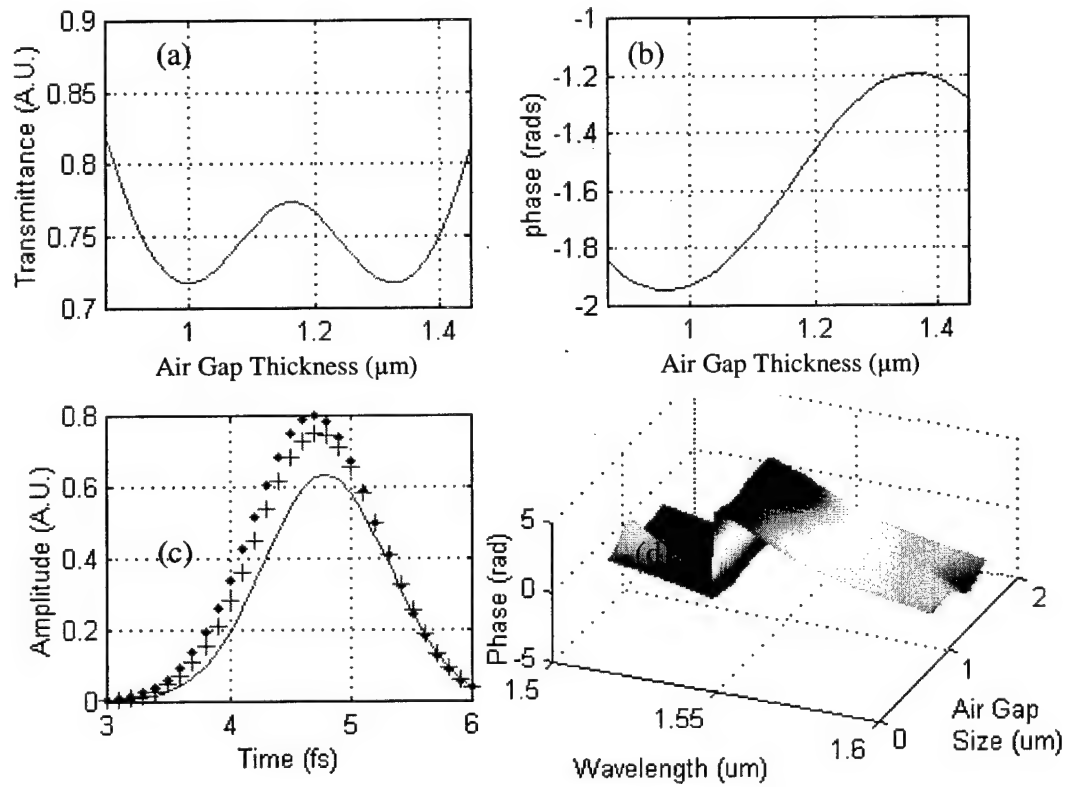


Figure 5-9: Calculated reflectance spectrum and output pulse of a filter with the structure $(\text{LH})^{12}\text{L}(\text{air})^2(\text{LH})^{11}\text{L}(\text{air})^2\text{L}$ quarter-wave layers where L and H represent the low and high index layers respectively. The material system used is $\text{Al}_{0.1}\text{Ga}_{0.9}\text{As}/\text{AlAs}$ on a GaAs substrate (a) Shows transmittance verses air gap thickness, (b) shows the transmittivity phase verses air gap thickness, (c) shows three output pulses when the position of the cantilever is moved from 1 μm (dotted) to 1.2 μm (+) to 1.4 μm (solid), (d) shows the transmittivity phase spectrum as the cantilever is moved.

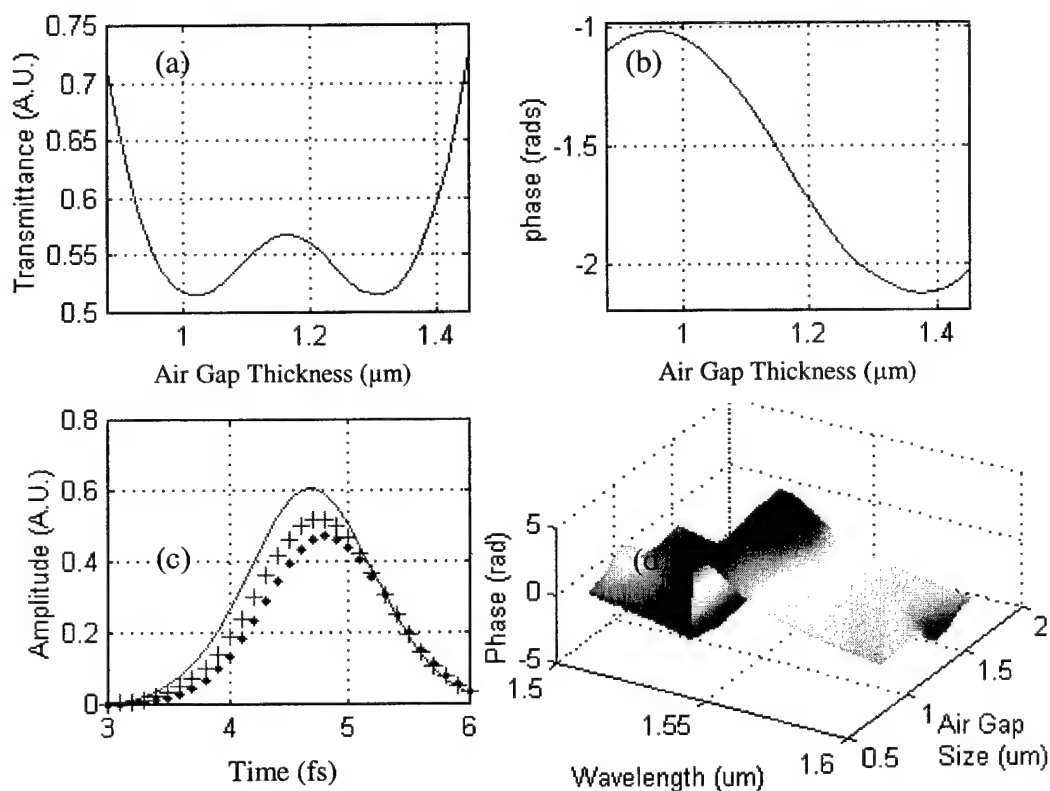


Figure 5-10: Calculated reflectance spectrum and output pulse of a filter with the structure $(\text{LH})^{14}\text{L}(\text{air})^2(\text{LH})^{11}\text{L}(\text{air})^2\text{L}$ quarter-wave layers where L and H represent the low and high index layers respectively. The material system used is $\text{Al}_{0.1}\text{Ga}_{0.9}\text{As}/\text{AlAs}$ on a GaAs substrate (a) shows transmittance verses air gap thickness, (b) shows the transmittivity phase verses air gap thickness, (c) shows three output pulses when the position of the cantilever is moved from 1 μm (dotted) to 1.2 μm (+) to 1.4 μm (solid). (d) shows the transmittivity phase spectrum as the cantilever is moved.

A structure containing 2 movable cantilevers and 4 air gaps was also designed using the computational algorithm described previously to give a maximum phase delay with cantilever position. The search criteria used was transmittance above 0.7, less than 11% change in transmittance when the cantilever position is varied and greater than 1.5 radians phase change. The theoretical matrix elements found were

$$0.4 \quad 1.27 \quad 0.29 \quad 1.35 \quad 0.3$$

This corresponded to an equivalent quarter-wave layered structure of

$$(LH)^2L(air)^3(LH)^{10}L(air)^2L(air)^3(LH)L(air)^3L$$

The transmittance and transmittivity phase results for the theoretical model is displayed in Figures 5-11 and 5-12. A maximum phase accumulation of 2.10 radians is produced with very high transmittance (above 0.89) and little fluctuation in transmittance. Figure 5-13 displays the transmittance, transmittivity phase, pulse delay and dispersion for the equivalent quarter-wave layered structure. The properties of this structure are significantly different to the theoretical model. The transmittance ranges from 0.53 to 0.61, which is much less than the theoretical model. The phase accumulation however is 2.63 radians, which is a 25% increase over the theoretical model.

There is some pulse dispersion in this structure. It is clearly indicated by the large change in the FWHM of the pulses shown in Figure 5-13(c). Figure 5-13(d) shows that the transmittivity phase curves significantly near the central wavelength of 1.55 μm which also indicates that this structure is dispersive. Further it suggests that the amount of dispersion varies with cantilever position.

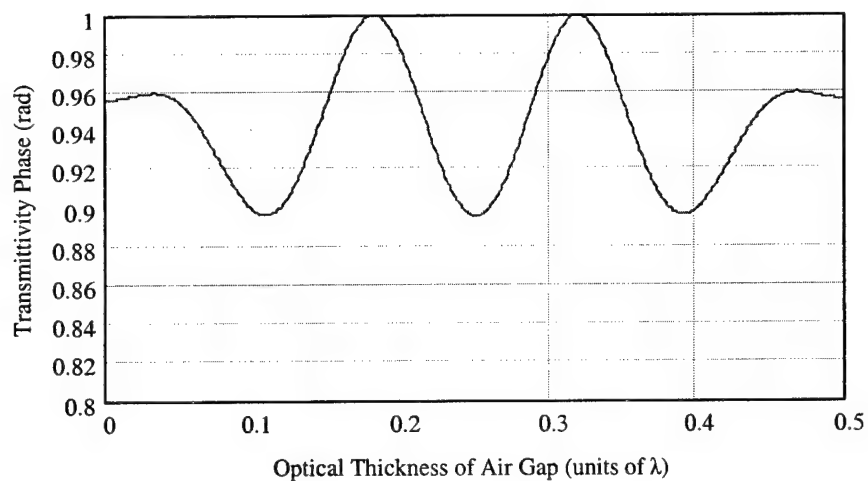


Figure 5-11: Transmittance spectrum of a filter using the 2x2 matrix elements (0.4 1.27 0.29 1.35 0.3). The material system used is $\text{Al}_{0.1}\text{Ga}_{0.9}\text{As}/\text{AlAs}$ on a GaAs substrate. The central wavelength is $1.55\text{ }\mu\text{m}$.

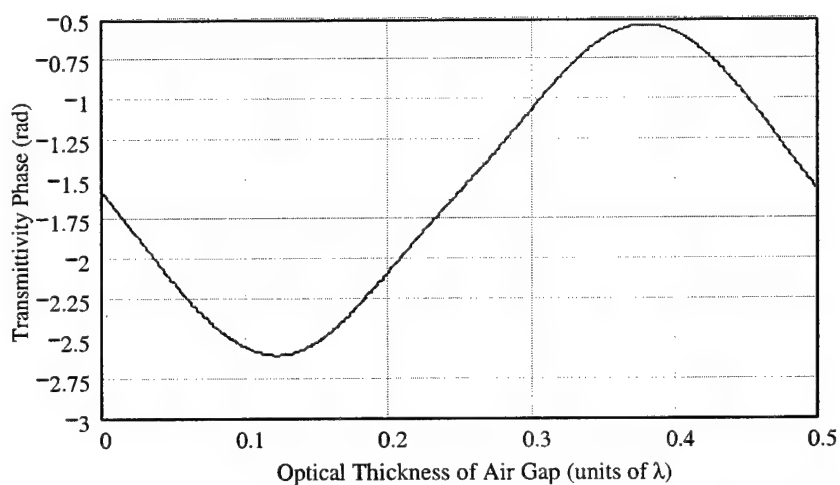


Figure 5-12: Transmittivity phase spectrum of a filter using the 2x2 matrix elements (0.4 1.27 0.29 1.35 0.3). The material system used is $\text{Al}_{0.1}\text{Ga}_{0.9}\text{As}/\text{AlAs}$ on a GaAs substrate. The central wavelength is $1.55\text{ }\mu\text{m}$.

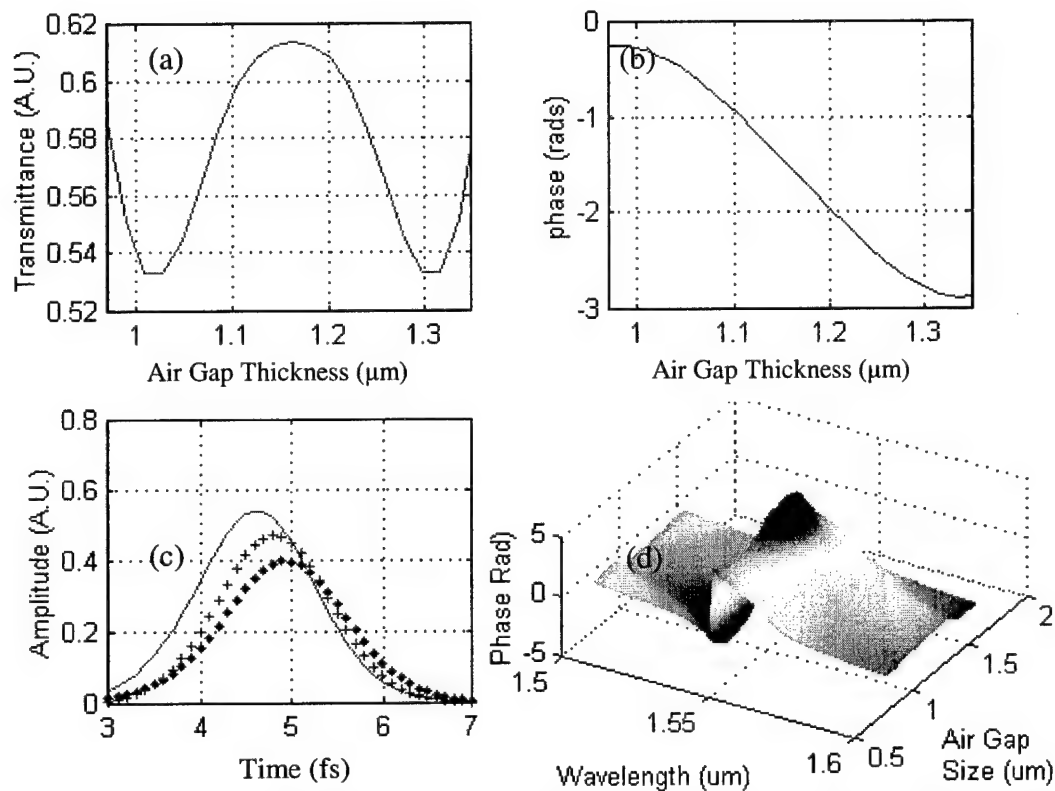


Figure 5-13: Calculated reflectance spectrum and output pulse of a filter with the structure $(LH)^2L(\text{air})^3(LH)^{10}L(\text{air})^2L(\text{air})^3(LH)L(\text{air})^3L$ quarter-wave layers where L and H represent the low and high index layers respectively. The material system used is $\text{Al}_{0.1}\text{Ga}_{0.9}\text{As}/\text{AlAs}$ on a GaAs substrate (a) shows transmittance verses air gap thickness, (b) shows the transmittivity phase verses air gap thickness, (c) shows three output pulses when the position of the cantilever is moved from 1.02 μm (dotted) to 1.22 μm (+) to 1.35 μm (solid). (d) shows the transmittivity phase spectrum as the cantilever is moved.

5.5 Variable Angle Structure

The structure used for this design is a $L((HL)^5H)^6(HL)^4H^5(HL)^4(H(HL)^4)^6$ optimized for 1.55 μm operation. The goal here is to maintain high transmittance with less than 10% variation while causing the same change in phase for both s- and p-polarized light. Figure 5-14 depicts the variation of transmittance and transmittivity phase when the structure is tilted through 65° . The transmittance is very high in both cases up to about 35° . After this point, the s- polarized light transmittance experiences large variations as the angle of incidence increases. The transmittivity phase looks very similar for both polarizations.

Figure 5-15 is a depiction of the difference between the transmittance and transmittivity phase of the s- and p- polarized light as the angle of incidence is increased from 0 to 65° . The difference in transmittance is less than 10% until an angle of incidence of 40° is reached. After that point the difference becomes wider and oscillatory in nature. The difference in transmittivity phase terms remain less than 2% up to that point.

Next, I propagate a pulse through the structure to access the level of dispersion in the p- and s- polarized pulses. Figure 5-16 depicts a p- polarized and s- polarized pulse propagating through the structure at an angle of incidence of 0 to 30 degrees. Both p- and s- polarized light pulses experience very little dispersion. Figure 5-16(b,d) shows that the transmittivity phase spectra appears linear near the central frequency of 1.55 μm . Hence no dispersion is observed.

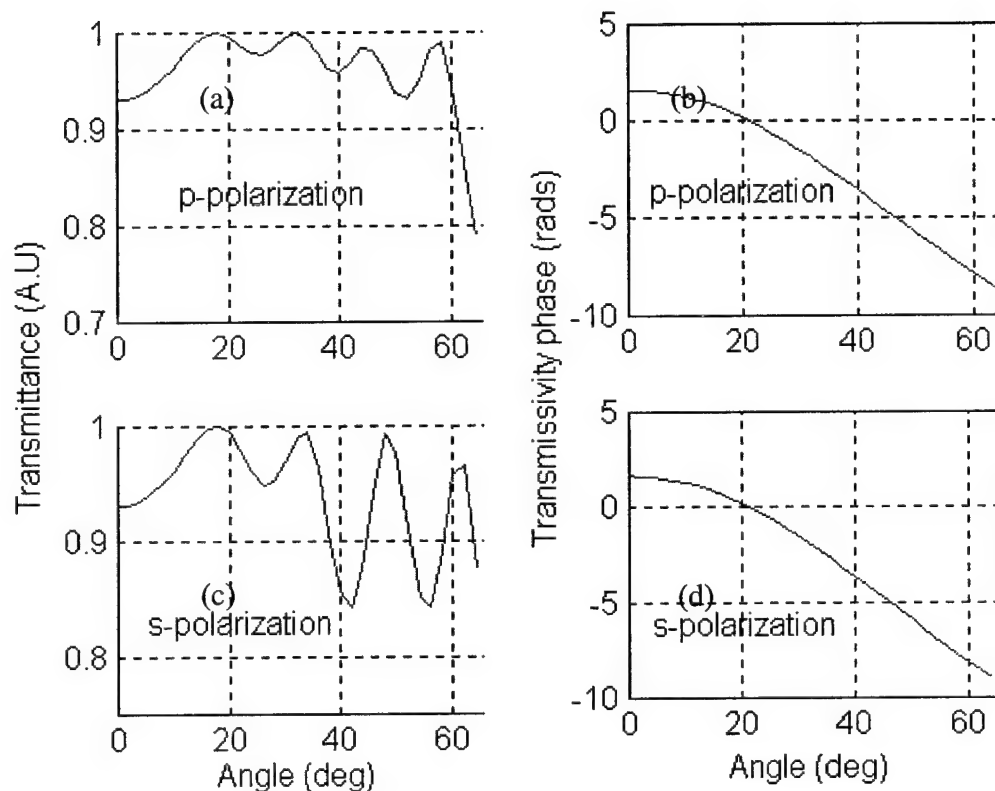


Figure 5-14: Calculated transmittance and transmittivity phase of a filter with the structure $L((HL)^5H)^6(HL)^4H^5(HL)^4(H(HL)^4)^6$ quarter-wave layers where L and H represent the low and high index layers respectively. The material system used is $Al_{0.1}Ga_{0.9}As/AlAs$ on a GaAs substrate. (a) and (c) are transmittance of p- and s- polarized light respectively. (b) and (d) are transmittivity phase of p and s polarized light respectively.

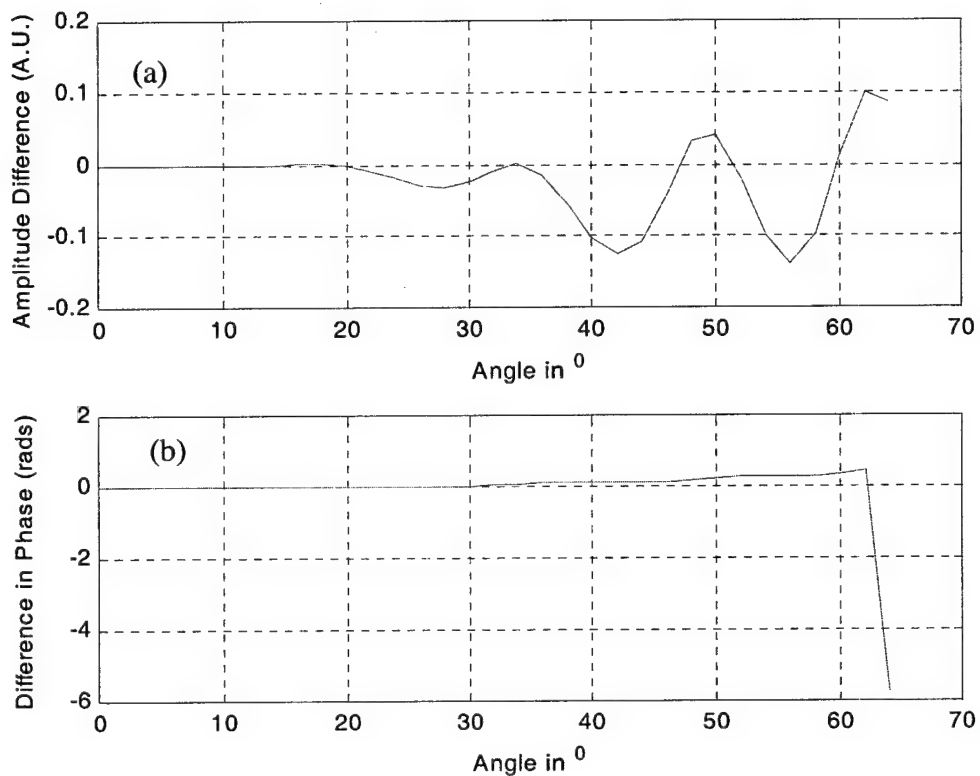


Figure 5-15: Calculated difference between transmittance and transmittivity phase of a filter with the structure $L((HL)^5H)^6(HL)^4H^5(HL)^4(H(HL)^4)^6$ quarter-wave layers where L and H represent the low and high index layers respectively, under p- and s- polarization. The material system used is $Al_{0.1}Ga_{0.9}As/AlAs$ on a GaAs substrate. (a) represents the difference in transmittance with angle and (b) represents the difference in phase with angle.

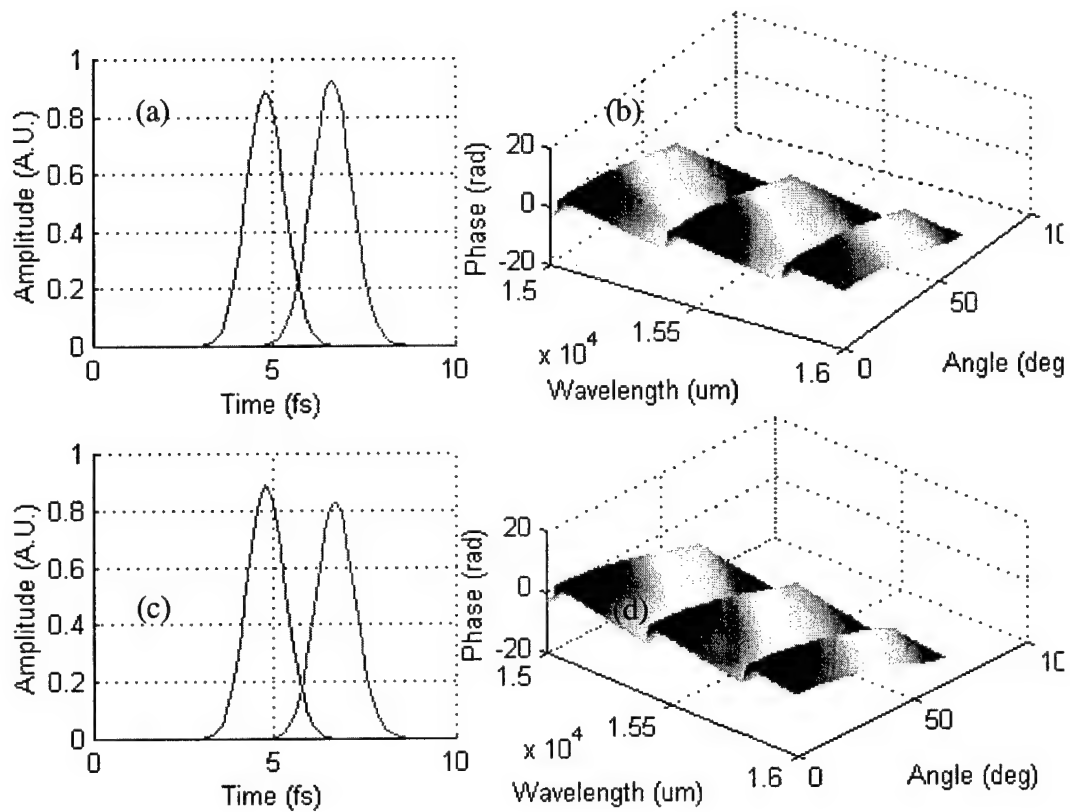


Figure 5-16: (a) Output pulse when a p- polarized pulse is incident at 0° (solid) and 60° (dotted). (c) represent the output pulse when a s polarized pulse is incident at 0° (solid) and 60° (dotted). (b) and (d) are the transmittivity phase spectra verses angle for (a) and (c) respectively.

When the pulses are propagated at a 30° angle of incidence, I expect the p and s-polarized pulses to have an amplitude of 0.99 and 0.95 based on the transmittance data. For the p polarized light, the amplitude is near 0.95 so a little distortion is experienced. However, the amplitude of the s polarized light is about 0.82, which indicates a significant amount of distortion has occurred.

In both the s and p cases, the delay experienced by the pulses increase linearly with the angle of incidence. A maximum delay of over 8 fs can be produced for both polarizations of light. However, for s polarized light, significant distortion will occur for any delay greater than 4 fs.

5.6 Summary

The structures designed all produced varying amounts of optical delay. The varying angle structures were able to produce the most phase accumulation, however, this is accompanied by increased distortion of the pulse. The QW structures were the second best performers, producing a little over 2π phase change with little dispersion. The best variable air-gap structure was a 4 air gap, 2 cantilever structure. It produced over 2.6 radians of phase accumulation. However, there was significant dispersion.

6.0 Conclusions and Recommendations

6.1 Introduction

In this chapter I summarize my research and compare the various methods I explored to introduce optical delay into semiconductor multilayer structures. I discuss the limitations of each method and propose improvements.

This research has several aspects that can be further developed. I will describe some areas of research that follow from this thesis.

6.2 Synopsis of Methods

The three methods of changing the optical delay presented in this thesis approach the task from very different perspectives. The embedded quantum well (QW) approach changes the optical thickness of selected layers within the structure to cause optical delay. This method is very attractive because it is fast, has no moving parts, and is easily integrated with other optoelectronic devices. It also produces very good theoretical results – about 2π of phase change under a maximum electric field of 50 kV/cm. However, this device can only operate in a narrow range of wavelengths from about 807 nm to 815 nm. Operating at lower wavelengths introduces absorption into the structure, which causes an unwanted insertion loss. Operating at higher wavelengths theoretically produces very little phase change because the change in refractive index due to an applied electric field is much smaller (less than 1%).

The second approach, using variable air gaps within the structure is also very attractive because it makes use of the evolving micro-electro-mechanical systems

(MEMS) technology that may become ubiquitous in the near future. This structure can be easily designed to operate at various wavelengths in any material system. The only requirement is that the passband must be above the band gap energy of the material layers to avoid unwanted absorption. However, the maximum modulation of optical phase delay calculated using the single and double air gap structures is less than π radians. Also, this structure is slower than the QW design and has moving parts that may break or degrade with time.

The third structure produced very good results (more than 2π modulation of phase with a 40 degree change in incident angle). However, more distortion was observed in this method than by using the other methods. Also, no viable means exists for implementing this technique in a practical system.

6.3 Possible improvements

There are several improvements for the structures I studied in this thesis. The filters used in the devices had sizable ripple in the passband. Though the amplitude was less than 10%, spike layers or other numerical methods can be used to suppress the ripple further. This would reduce distortion in pulses propagating through the structure.

To make the calculation of the structures for the variable air gap device tractable, I searched for only quarter-wave layers in my algorithm. This may have negatively impacted my results. Allowing the routine to search for solutions, which contain non- $\lambda/4$ layers, could produce better results.

Finally, work needs to be done to determine what amount of pulse distortions is acceptable in multilayer structures for use in communications and other applications.

6.4 Recommendations for Further Research

This field of research is very young and there are many areas that can be further investigated. Initially, uncoupled QWs were used in the first structures investigated. However, with the aid of wavefunction engineering it was found that coupled quantum wells with certain characteristics produced better results than the single quantum well structures. Further work can be done to improve on the coupled quantum well design by considering wavefunction interactions. Also, the material system used by Feng only allowed design in the 810 nm wavelength range. Research can be done using InGaAs wells or other materials to produce a structure that can operate at longer wavelengths.

There is still more work to be done with the variable air-gap structure. The effects of using six or more air gaps can be investigated to determine if more phase change can be introduced by varying the position of the cantilevers. Working with non- $\lambda/4$ layer structures can also be investigated. This may produce better results for the structures already analyzed above.

Finally, the structures presented in this thesis can be fabricated and tested to verify the theoretical results I presented in this thesis.

Vita

Second Lieutenant Michael I. K. Etan was born on the island of Saint Lucia in the Eastern Caribbean. He graduated from the Vieux Fort Comprehensive School in 1988 and from the Sir Arthur Lewis Community College in 1990 both in Saint Lucia. He immigrated to the United States in 1991.

He enlisted in the United States Air Force in March 1992. His first assignment was to Chanute AFB, Illinois where he was named an honor graduate in August 1992 at the Weather Specialist School. His second assignment was to the 42nd Operation Squadron at Maxwell AFB, Alabama where he served as a Weather Observer.

He became a citizen of the United States in January 1996 and was awarded a scholarship under the SOAR program to attend Purdue University in Indiana in 1996. He graduated from Purdue University in 1999 with a Bachelor of Science degree in Electrical Engineering. He was commissioned in May 1999 through ROTC Detachment 220 at Purdue.

His first duty assignment beginning in August 1999 was to attend the Air Force Institute of Technology, Wright-Patterson AFB, Ohio to earn a masters degree in electrical engineering. Upon graduation in March 2001, he will report to the Air Intelligence Agency at Kelly Air Force Base in San Antonio, Texas.